MSDE

PAPER

View Article Online
View Journal | View Issue

Cite this: *Mol. Syst. Des. Eng.*, 2024, **9**, 625

Tuning the photophysical properties of ESIPT active unsymmetrical azine dyes by the change in the substituent and solvent: TD-PBE0 and TD-CAM-B3LYP studies†

Hossein Roohi * and Tahereh Pouryahya

Received 1st March 2024,
Accepted 26th March 2024

DOI: 10.1039/d4me00039k

rsc.li/molecular-engineering

In this study, the effects of the substituent and solvent on the photophysical properties of the designed ESIPT active as well as donor–acceptor structured unsymmetrical azine dyes **L1**–**L5** (R1–5 = –H, $–NH_2$, $–OCH_3$, $–CF_3$ and –CN, respectively) were investigated at PBE0/6-31++G(d,p) and CAM-B3LYP/6-31++G(d,p) levels of theory in the gas phase and three solvent media. The structural parameters, relative energies, vibrational spectra, photophysical properties, potential energy curves, natural bond orbital (NBO) charges, charge transfer (CT) indices, electron density properties, and reduced density gradient (RDG) spikes were computed. The results of vibrational spectra, structural parameters and electron density analysis demonstrated that the O–H···N H-bonding interaction is strengthened in all dyes upon photoexcitation from the S_0 to S_1 state which can facilitate the ESIPT process. All dyes exhibited both enol and keto emissions, in good agreement with the reported experimental results. The largest Stokes shift for keto emissions in solvent media was observed in MeOH solvent and is in the order 143 nm (**L5**) > 138 (**L4**) > 133 (**L1**) > 120 (**L3**) > 115 (**L2**) at the PBE0/6-31++G(d,p) level of theory. Introducing electron-withdrawing groups can increase the absorption and emission wavelengths as well as the red shift in fluorescence emission of **L4** and **L5**, but hinder the occurrence of the ESIPT process compared with **L2** and **L3**. The results demonstrated that the substituent effect is more significant in changing the molecular optical properties than the solvent effect. Our designed ESIPT molecules can simultaneously show enol and keto emissions and thus can be regarded as candidates to design single-molecule white-light emission materials.

Design, System, Application

Azines are a class of Schiff base compounds that undergo a wide variety of chemical processes and have interesting optical properties. Particularly, ESIPT-active symmetrical and unsymmetrical azines coupled with AIE units have been developed and applied in cell imaging, fluorescent probes for the detection of cations, antibacterial activity and textile applications. The photophysical properties of azine dyes can be tuned by substitution on the ESIPT moiety. In this work, we have utilized a quantum engineering strategy for designing a suitable molecular photo-switch based on azine derivatives. It was found that all dyes exhibit double enol and keto fluorescence emissions.

1. Introduction

Luminescent organic materials exhibiting the unique excited-state intramolecular proton transfer (ESIPT) process have technological and biological roles in applications such as fluorescent probes,[1–7] organic light-emitting diodes (OLEDs),[8–11] laser dyes[12,13] and drug delivery systems (DDSs) or bioactive donors.[14,15] Since the ESIPT mechanism was first reported in an experimental study in methyl salicylate by Weller,[16] numerous investigations have been performed experimentally and theoretically due to its special photophysical and photochemical properties.[17–21] ESIPT molecules feature an intramolecular hydrogen bond between the proton donor (–OH, $–NH_2$) and the proton acceptor (–C═O, –C═N–) groups close to each other allowing proton transfer to occur upon photoexcitation. Generally, ESIPT is a kind of enol–keto phototautomerization in which the excited molecule undergoes a proton transfer process, resulting in the formation of a new tautomeric form. Some ESIPT chromophores show dual emissions, short wavelength emission due to the enol form (normal emission), and a longer one due to the keto form (ESIPT emission) through

Department of Chemistry, Faculty of Science, University of Guilan, P.O. Box 98135-674, Rasht, Iran. E-mail: hroohi@guilan.ac.ir; Fax: +981313220066; Tel: +981313243630 35

† Electronic supplementary information (ESI) available. See DOI: https://doi.org/10.1039/d4me00039k

the photocycle. The single ESIPT happens in a four-level photocycle including absorption, ESIPT, emission, and ground-state intramolecular proton transfer (GSIPT). Large Stokes shifts, tunable and dual emission, ultrafast processes, and spectral sensitivity to the environment conditions are the desirable properties of ESIPT fluorophores.[22–25] ESIPT fluorophores have long been attractive as solid-state emitters and this interesting characteristic can be achieved by the introduction of ESIPT centers on the core of aggregation-induced emission (AIE) dyes.[26]

Azines are a class of Schiff base compounds that undergo a wide variety of chemical processes and have interesting optical properties.[27,28] Particularly, ESIPT-active symmetrical and unsymmetrical azines coupled with AIE units have been developed and applied in cell imaging,[29,30] fluorescent probes for the detection of cations,[31,32] antibacterial activity[33] and textile applications.[34] Both ESIPT and AIE processes can be found in salicylaldehyde azines and Schiff bases, leading to efficient emission and large Stokes shifts in the solid state. Tong *et al.*[35] have developed an alternative building block, keto-salicylaldehyde azine (KSA), for constructing various AIEgens *via* an ESIPT process to detect some cellular organelles and specific metal ions. They have shown that their intrinsic electronic structure can be easily affected by the asymmetric substitution effect. Mathivanan and coworkers designed and synthesized donor–acceptor-structured triphenylamine (TPA) functionalized unsymmetrical azines containing various salicylaldehyde derivatives which exhibited intramolecular charge transfer (ICT), ESIPT and tuned multi-color AIE features.[36] By changing the electron-donating ability at the ESIPT moiety, they could tune the optical properties of these newly synthesized molecules. All compounds exhibited the AIE behavior in a THF/water mixture and the ESIPT. In addition, different emission colors in the aggregated state were observed by the tuning of a peripheral substituent in the salicylaldehyde moiety. The crystal structure of the molecules confirmed the existence of strong intramolecular hydrogen bonding between the imine nitrogen C=N and phenolic OH groups, which promotes the ESIPT process in the excited state. In addition, Mathivanan *et al.*[33] have also reported the synthesis of four donor–acceptor structured symmetrical triphenylamine supported bis unsymmetrical azine derivatives. They have found that all compounds show interesting solvatochromic features and substituent-dependent multi-color aggregation-induced emission behavior in a THF–water mixture. The experimental results confirmed AIE behavior in the compounds and it might be due to the restriction of the intramolecular rotation (RIR) mechanism.

The excited state hydrogen bonding dynamics and excited state intramolecular proton transfer (ESIPT) mechanism of a salicylaldehyde derivative with a *para*-position electron-withdrawing cyano group (CN-SAA) have been explored.[37] It has been demonstrated that dual intramolecular hydrogen bonds of CN-SAA can be enhanced in the S_1 state and charge reorganization plays an important role in promoting ESIPT behavior for CN-SAA. In another study, four organic fluorophores with two intramolecular H-bonding functionalities and unsymmetrical structures (salicylaldehyde–imine and benzophenone–imine) have been designed and explored.[38] All dyes showed tunable solid-state fluorescence between 536 and 645 nm dependent on inter/intramolecular H-bonding interaction. Four novel salicylaldehyde–diphenyl–azine (SDPA) skeleton-based luminogens with tunable emission have been synthesized by Jain *et al.*[39] The photophysical studies in different solvents elucidated their ESIPT and AIE characteristics. Also, this study demonstrated that changing the substituents on the salicylaldehyde does not affect the selectivity and sensitivity towards Cu^{2+} ions. Instead, this significantly tunes emission properties towards the longer wavelength region. Recently,[40] a comprehensive photophysical study of a novel unsymmetrical monosubstituted salicylaldehyde azine-based organic functional molecule named 4-chloro-2-((*E*)-((*E*)-(pyren-1-ylmethylene)hydrazono)methyl)phenol (PHCS) has been reported. A prevalence of the synergistic effect of aggregation-induced emission enhancement (AIEE) and ESIPT in the PHCS molecular system has been rationalized at extremely high water concentrations compared to organic solutions with low to moderate water concentrations.

However, the information on ESIPT dynamics and the effect of the substituent as well as solvent on the ESIPT process of unsymmetrical azine derivatives cannot be provided by the current spectroscopic techniques. Computational chemistry as a reasonable and reliable tool can be used to deeply explore the mechanism of ESIPT at the molecular level. Theoretical studies on the mechanism of ESIPT-based chromophores not only help the researcher to understand the underlying mechanism for tuning the fluorescence behavior but also provide a theoretical guide for further developing new ESIPT-based dyes. Despite the reported experimental research on salicylaldehyde azine-based ESIPT dyes, based on the best of our knowledge, there was no detailed study conducted on the mechanism of ESIPT and the origin of the changes in photophysical properties of unsymmetrical azines containing various salicylaldehyde derivatives as the acceptor group and triphenylamine as the donor one in various solvents. The study of the ESIPT mechanism can provide insights into the design of materials with desired electronic and photophysical properties. Accordingly, in this work, we have investigated the excited state mechanism and photophysical properties of five ESIPT-based salicylaldehyde azine derivatives.

We have previously reported the influence of different substituents on the ESIPT reactions of a series of coumarin–benzothiazole derivatives based on theoretical calculations.[41] In this study, we have explored the ESIPT mechanism and the effect of the substituent and solvent on the photophysical properties of the designed **L1–L5** azine-based dyes (Scheme 1) by using the density functional theory (DFT) and the time-dependent density functional theory (TD-DFT) approaches at PBE0/6-31++G(d,p) and CAM-B3LYP/6-31++G(d,p) levels of theory in the gas phase and three solvents with

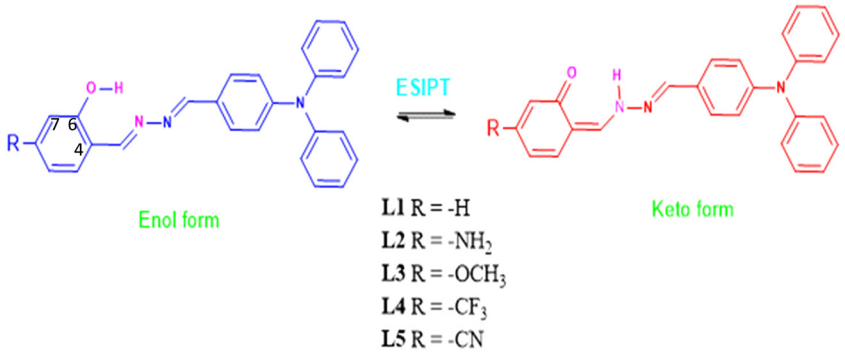

Scheme 1 Eno1–keto tautomerism and chemical structures of **L1**–**L5** compounds.

various polarities. In the main synthesized[36] molecule **L1**, triphenylamine is a well-known π-electron-donating group with high donor tendency, and salicylaldimine (SAI) is a common acceptor as well as an ESIPT-active unit. All the compounds possess the main donor (TPA)–acceptor (SAI) structure with additional substituents (–H, $–NH_2$, $–OCH_3$, $–CF_3$, and –CN) on the proton donor part. In the designed **L2**–**L5** molecules, since the electron-donating TPA group is located on the proton acceptor side, the introduction of electron-donor and acceptor substituents at the proton donor side can more significantly cause the push/pull substituent effect on electrons, thereby tuning the ESIPT reaction as well as photophysical properties. The study of the ESIPT mechanism can provide insights into the design of materials with desired electronic and photophysical properties. The purpose of the current work is to design and develop azine-based ESIPT molecules with potential applications in light-emitting diodes, optical sensors and optoelectronic devices. In addition, our designed ESIPT molecules can simultaneously show two emission bands, including enol-form and keto-form emissions, and thus can be regarded as candidates to design single-molecule white-light emission materials owing to the combination of the dual emission of enol/keto forms.

2. Computational details

Time-dependent density functional theory (TD-DFT) has become a popular tool for computing the signatures of electronically excited states, and more specifically, the properties directly related to the optical (absorption and emission) spectra of molecules.[42] The density functional theory[43,44] and the time-dependent density functional theory (TDDFT)[45] have been employed in the S_0 and the S_1 states, respectively. In this work, the experimental data of absorption and emission for **L1** (ref. 36) were considered as a benchmark to validate CAM-B3LYP[46] and PBE0 (ref. 47) functionals in conjunction with the 6-31++G(d,p) basis set.[48] The ground and first excited state optimized geometries were computed by using the PBE0 (consisting of 25% of the exact exchange of HF) and CAM-B3LYP (long-range-corrected version of the B3LYP hybrid functional consisting of 19–65% of the exact exchange of HF) functionals in conjunction with the 6-31++G(d,p) basis set using the Gaussian 16 program package.[49]

The selection of exchange–correlation (XC) functionals incorporating different fractions of Hartree–Fock (HF) exchange is based on the recognized influence of HF exchange on excitation energies[50–52] and oscillator strengths.[52–55] The CAM-B3LYP functional is a long-range-corrected version of the B3LYP hybrid functional, while PBE0 mixes the PBE exchange energy and Hartree–Fock exchange energy in a set 3 : 1 ratio, along with the full PBE correlation energy. The main difference between the two functionals is the way they handle the exchange–correlation energy. CAM-B3LYP uses a different switching function than B3LYP, while PBE0 mixes the PBE exchange energy and Hartree–Fock exchange energy. Both functionals have been shown to be accurate in DFT calculations, but the choice of functional depends on the specific system being studied and the desired level of accuracy. The reported photophysical results revealed that for both local n → π* and π → π* transitions, global hybrids such as PBE0 will generally provide accurate estimates whereas for CT or Rydberg EES, it is mandatory to use range separated hybrids (recommended CAMB3LYP or wB97X-D) to reach physically meaningful estimates.[42,45] Therefore, a direct comparison of the results of CAM-B3LYP and PBE0 functionals can provide insights into the application of these functionals in luminescence property calculations.

The absorption and emission spectra were calculated by using both functionals at TD-DFT/6-31++G(d,p)//DFT/6-31++G(d,p) and TD-DFT/6-31++G(d,p) levels of theory, respectively. The vertical absorption E(vert-abs) and vertical fluorescence E(vert-flu) energies are calculated by the following equations:[42]

$$E(\text{vert-abs}) = E^{\text{EES}}(R^{\text{GS}}) - E^{\text{GS}}(R^{\text{GS}}) \quad (1)$$

$$E(\text{vert-flu}) = E^{\text{EES}}(R^{\text{ES}}) - E^{\text{GS}}(R^{\text{ES}}) \quad (2)$$

where $E^{\text{EES}}(R^{\text{ES}})$ is the energy of the excited state at the ground state geometry, $E^{\text{GS}}(R^{\text{GS}})$ is the energy of the optimized ground state, $E^{\text{EES}}(R^{\text{ES}})$ is the energy of the optimized excited state and $E^{\text{GS}}(R^{\text{ES}})$ is the energy of the ground state at the excited state geometry.

Dimethylsulfoxide (DMSO: ε = 46.826), methanol (MeOH: ε = 32.613) and toluene (ε = 2.3741) solvents were selected to study the effect of solvent polarity on the absorption and fluorescence radiation based on the polarizable continuum model (PCM).[56] To further investigate the ESIPT process, the potential energy curves (PECs) along the proton transfer path were constructed by freezing the O–H coordinate to a series of values and then optimizing the rest of the coordinates using the PBE0 method at the S_0 state and the TD-PBE0 method at the S_1 state.[42,57,58] To characterize the hydrogen bonds with different strengths, the quantum theory of atoms in molecules (QTAIM) analysis[59,60] was performed at the

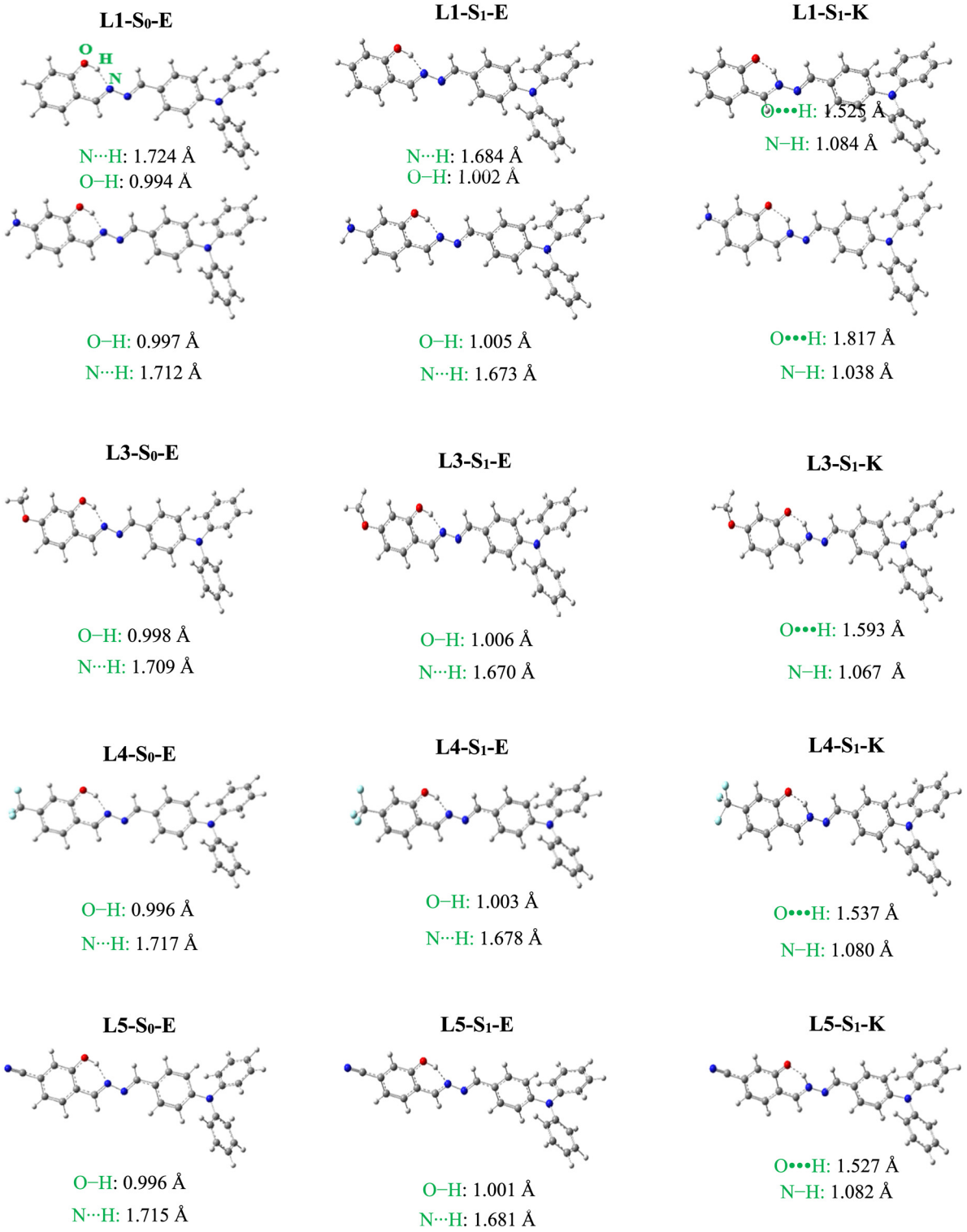

Fig. 1 The PBE0 optimized structures of **L1**–**L5** at S_0 and S_1 states (the key bond lengths in Å are also shown).

PBE0/6-31++G(d,p) level of theory by using the AIM2000 program package.[61] Besides, for revealing the intramolecular hydrogen bonding interactions in real space and to compare the hydrogen bond strength, the reduced density gradient (RDG) isosurfaces[62] were calculated using Multiwfn software[63] and plotted using the (VMD) program.[64] Analysis of charge transfer during electron excitation based on the electron density difference (EDD)[65] was done using Multiwfn software. The natural bond orbital (NBO) analysis[66,67] was carried out at the PBE0/6-31++G(d,p) level to realize the charge distributions during the ESIPT process.

3. Results and discussion

3.1. Geometric structures

Fig. 1 shows the geometric structures of azine derivatives **L1**–**L5** (R1–5 = –H, $–NH_2$, $–OCH_3$, $–CF_3$, and –CN) in enol (E) and keto (K) forms at S_0-E, S_1-E and S_1-K states at the PBE0/6-311++G(d,p) level. Intramolecular hydrogen bond (IHB) interactions are the important driving force of the ESIPT reaction in a molecule. Thus, for a deeper understanding of the proton transfer behavior, the main parameters such as the bond length and bond angle involved in the hydrogen bonds in the S_0 and S_1 states were calculated and are reported in Table 1. For **L1**–**L5**, the O–H bond length at the S_0-E state is in the order **L3** (0.998 Å) > **L2** (0.997 Å) > **L4** and **L5** (0.996 Å) > **L1** (0.994 Å). The order of the O–H···N H-bonding distance is **L1** (1.724 Å) > **L4** (1.717 Å) > **L5** (1.715 Å) > **L2** (1.712 Å) > **L3** (1.709 Å). The δ(O–H···N) bond angle can be arranged in the following order: **L2** (147.8°) > **L3** (147.7°) > **L1** (147.2°) > **L5** and **L4** (147.1°). Based on the structural parameters, the strength of IHB interaction in the S_0-E state molecules can be arranged as follows: **L3** ($–OCH_3$) > **L2** ($–NH_2$) > **L5** (–CN) > **L4** ($–CF_3$) > **L1** (–H). The O···N distance in the O–H···N H-bonding structure for **L1** to **L5** at the S_0-E state is 2.616, 2.611, 2.607, 2.610 and 2.608 Å, respectively. The shortest O···N and H-bonding distance corresponds to the **L3** molecule with the electron-donating $–OCH_3$ substituent.

Table 1 The main bond lengths (Å) and angles (degree) of **L1**–**L5** (R1–5 = –H, $–NH_2$, $–OCH_3$, $–CF_3$, and –CN) calculated at the PBE0/6-31++G(d,p) level at the S_0 and S_1 states

	State	O–H	N–H	δ(O–H–N)	N–O
L1	S_0-E	0.994	1.724	147.2	2.616
	S_1-E	1.002	1.684	149.4	2.597
	S_0-K	1.555	1.075	142.7	2.496
	S_1-K	1.525	1.084	145.7	2.496
L2	S_0-E	0.997	1.712	147.8	2.611
	S_1-E	1.005	1.673	149.7	2.591
	S_0-K	1.601	1.065	141.0	2.519
	S_1-K	1.817	1.038	136.3	2.666
L3	S_0-E	0.998	1.709	147.7	2.607
	S_1-E	1.006	1.670	149.7	2.588
	S_0-K	1.626	1.059	140.0	2.530
	S_1-K	1.593	1.067	143.3	2.531
L4	S_0-E	0.996	1.717	147.1	2.610
	S_1-E	1.003	1.678	149.4	2.592
	S_0-K	1.571	1.071	142.1	2.504
	S_1-K	1.537	1.080	145.3	2.501
L5	S_0-E	0.996	1.715	147.2	2.608
	S_1-E	1.001	1.681	149.3	2.593
	S_0-K	1.550	1.076	143.0	2.494
	S_1-K	1.527	1.082	145.4	2.495

The comparison of geometric parameters reveals the changes in IHB strength after the photoexcitation process. As seen in Table 1, for **L1**–**L5**, the O–H bond length and δ(O–H···N) bond angle increase, whereas the N···H and N···O bond lengths decrease after the photoexcitation process. The O–H bonds of **L1**–**L5** (R1–5 = –H, $–NH_2$, $–OCH_3$, $–CF_3$, and –CN) are elongated from 0.994, 0.997, 0.998, 0.996 and 0.996 Å at the S_0-E state to 1.002, 1.005, 1.006, 1.003 and 1.001 Å at the S_1-E state, respectively. The N···H H-bond distance is 1.724, 1.712, 1.709, 1.717 and 1.715 Å at the S_0-E state which decreases to 1.684, 1.673, 1.670 and 1.678 and 1.681 Å at the S_1-E state, respectively. The decrease in the N···H H-bond distance upon photoexcitation is 0.040, 0.039, 0.039, 0.039 and 0.034 Å in **L1**–**L5**, respectively. The O···N distance is also reduced by 0.019, 0.019, 0.019, 0.018 and 0.016 Å upon excitation from S_0-E to S_1-E. A decrease in the O···N distance makes the H-bonded ring smaller in the S_1-E state than in the S_0-E one and, in turn, makes S_1-E unstable and proton transfer faster. The δ(O–H···N) bond angle in **L1**–**L5** increases from 147.2, 147.8, 147.7, 147.1 and 147.2° at the S_0-E state to 149.4, 149.7, 149.7, 149.4 and 149.3° at the S_1-E state, respectively. These results show that the intramolecular hydrogen bond is strengthened at the S_1 state which can facilitate the occurrence of the proton transfer process. Based on hydrogen bond structural parameters, it is predicted that the strength of IHB interaction at the S_1-E state is in the order **L3** ($–OCH_3$) > **L2** ($–NH_2$) > **L4** ($–CF_3$) > **L5** (–CN) > **L1** (–H).

In addition, to judge the configurational changes of molecules going from the S_0-E state to the S_1-E one, the optimized structures of the molecules at the S_0 and S_1 states were evaluated by root mean square deviation (RMSD). Greater RMSD implies greater structural changes during the photoexcitation. Analysis of RMSD showed that its value is more sensitive to dihedral angles of the donor part of molecules than to bond lengths and bond angles. The RMSD values for the structural changes of the **L1**–**L5** molecules at the PBE0/6-31++G(d,p) level of theory are 5.88, 4.95, 5.2, 7.25 and 37.8, respectively. Its value at the CAM-B3LYP/6-31++G(d,p) level of theory is 1.02, 0.73, 0.86, 1.23, and 29.38, respectively, that is, lower than those calculated using the PBE0 functional; the predicted trend of both functionals is the same. These results indicate that the RMSD value for the **L4** and **L5** molecules with electron-withdrawing substituents is greater than those found for the **L1**–**L3** molecules. Besides, the structural variations between S_0 and S_1 states can correlate with the normal emission wavelength of molecules which will be discussed in the next section.

The O–H···N H-bonding at the S_1-E state is switched by O···H–N H-bonding at the S_1-K state upon the ESIPT process. In the S_1 excited state, the O···HN H-bond distance corresponding to the S_1-K form of **L1**, **L2**, **L3**, **L4** and **L5** is

1.525, 1.817, 1.593, 1.527 and 1.537 Å, respectively, indicating that the strength of IHB decreases as follows: **L1** (–H) > **L4** (–CF_3) > **L5** (–CN) > **L3** (–OCH_3) > **L2** (–NH_2). The H-bond distance in the S_1-K (O···H–N) forms of **L1–L5** is smaller than those found for the S_1-E (O–H···N) forms (except for **L2**). This reveals that O···H–N H-bonding in the keto form is stronger than the O–H···N one in the enol form at the S_1 state. The values of the δ(O–H···N) bond angle at the S_1-K form of **L1**, **L2**, **L3**, **L4** and **L5** are 145.7, 136.3, 143.3, 145.4 and 145.3°, respectively, which are smaller than those at the S_1-E form.

The variations of the (N–H and O···N) bond distances and δ(O–H···N) bond angle *versus* RC (RC = d_{OH}) along the proton transfer pathway of selected **L1–L5** molecules at the S_1 state are illustrated in Fig. 2. The graphs in the S_0 state are shown in Fig. S1 of the ESI.† The plots of the variations of the (O···N) distance and δ(O–H···N) angle are similar in both states, but the O···N distance is different in the crossover point (COP) of the ground and excited states. As can be observed, the O···N distance first decreases to a minimum and the δ(O–H···N) bond angle increases to a maximum in the COP before the proton transfer occurs. The COP between the enol and keto forms of **L1** to **L5** is located at R(O–H) = 1.300, 1.305, 1.306, 1.303 and 1.301 Å at the S_1 state, respectively. At the COP, the O···N distance in the **L1–L5** is 2.430, 2.422, 2.421, 2.420 and 2.419 Å so that **L5** with the electron-withdrawing –CN group shows the shortest O···N distance at the COP. All of these intrinsic distortions in the structures happen to facilitate the proton transfer in the first S_1 excited state.

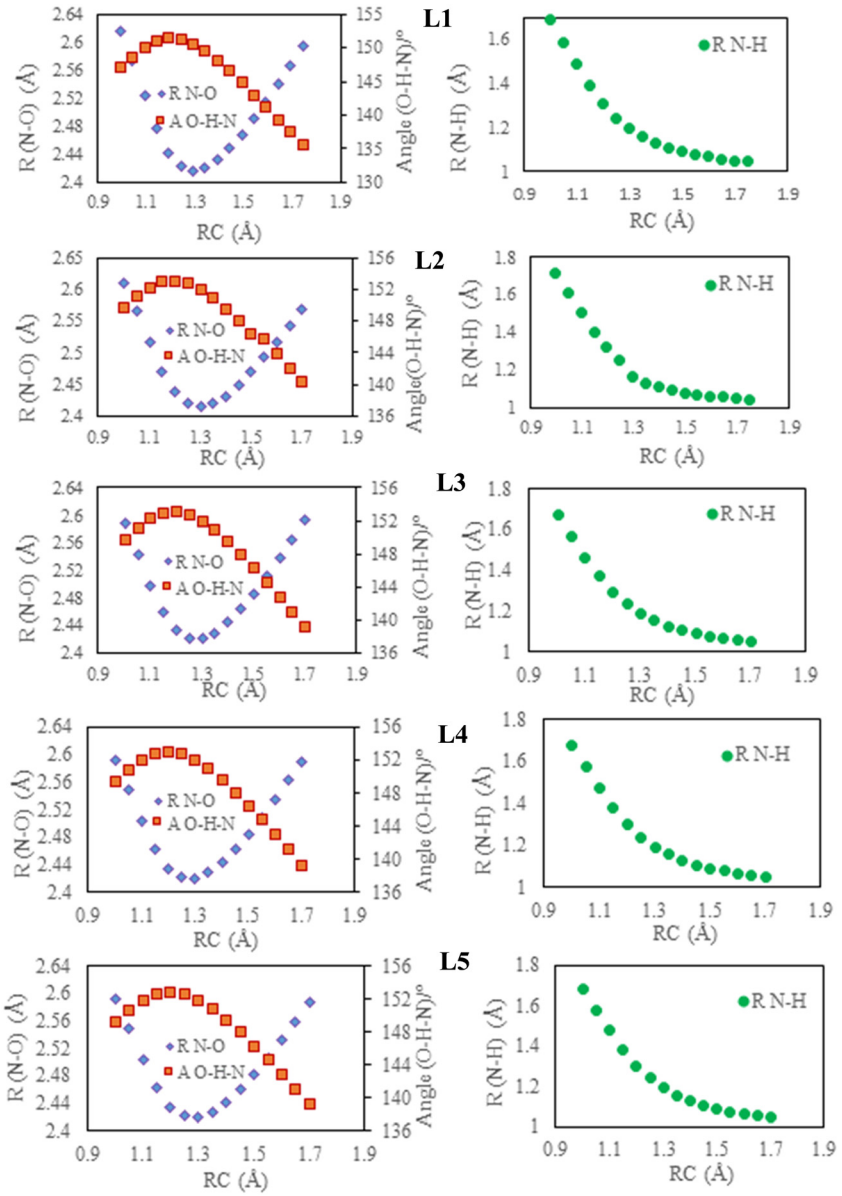

Fig. 2 Variations of the N–H and O–N bond distances and O–H–N bond angle *versus* RC (d_{OH}) along the proton transfer path for **L1–L5** (R1–5 = –H, –NH_2, –OCH_3, –CF_3, and –CN) in the S_1 state at the PBE0/6-31++G(d,p) level.

3.2. Relative energies

The relative energies of the optimized structures in the gas phase and solvent media at the PBE0/6-31++G(d,p) level are given in Table 2 and those at the CAM-B3LYP/6-31++G(d,p) level are listed in Table S1 of the ESI.† In the gas phase, at the ground state, the keto forms of **L1–L5** (R1–5 = –H, $–NH_2$, $–OCH_3$, $–CF_3$, and –CN) are less stable than the enol forms due to the higher energies. Compared with S_0-E, the energies of the S_0-K forms for **L1–L5** are 7.46, 6.14, 5.63, 6.87 and 7.03 kcal mol^{-1} based on the PBE0 and 8.67, 7.13, 6.57, 8.08, and 8.30 kcal mol^{-1} based on the CAM-B3LYP functional. The S_1-(FC) states of **L1–L5** are 69.04, 69.64, 69.58, 66.43 and 63.89 kcal mol^{-1} using the PBE0 and 81.44, 80.97, 81.25, 79.84 and 78.35 kcal mol^{-1} based on the CAM-B3LYP functional higher than the S_0-E state. In addition, compared with S_0-E, the S_1-E state energy of the five **L1–L5** molecules is predicted to be 61.10, 64.04, 63.05, 57.29 and 55.10 kcal mol^{-1} by using PBE0 and 75.42, 74.90, 75.13, 73.91 and 72.45 kcal mol^{-1} based on the CAM-B3LYP method, respectively. Therefore, it can be concluded that the conversion of S_1-(FC) to S_1-E in **L1–L5** is an exergonic process by releasing the energy of −7.94, −5.60, −6.53, −9.14 and −8.79 kcal mol^{-1} based on PBE0 and −6.02, −6.07, −6.12, −5.93 and −5.9 kcal mol^{-1} by using the CAM-B3LYP method. The formation of the keto tautomers is driven by the difference in energy between the S_1-(FC) and keto structures at the S_1 state. The results in Tables 2 and S1† show that for all compounds, the PBE0 method provides a smaller energy difference between the two S_1-(FC) and S_1-K states of **L1** (−2.44), **L2** (−3.13), **L3** (−2.66), **L4** (−4.02) and **L5** (−3.43 kcal mol^{-1}) compared with the CAM-B3LYP method, which is **L1** (−5.04), **L2** (−3.22), **L3** (−4.34), **L4** (−4.48) and **L5** (−4.05 kcal mol^{-1}). However, these results indicate that the proton transfer for all azine derivatives is an exergonic process at the S_1 state. A comparison of relative energies calculated using the two functionals demonstrates that the CAM-B3LYP energies are greater than the PBE0 ones.

Fig. 3 shows the schematic energy diagram of the photo-tautomerization for the **L1–L5** molecules in the gas phase. In the ground state, the dyes are mostly stable in the enol (S_0-E) form. Excitation of this form by photons leads to the transition of the molecules to the Franck–Condon excited state S_1-E(FC), which rapidly decays to the local enol form (S_1-E) minimum. There are two deactivation paths from the minimum of S_1-E. The excited molecules can immediately undergo the ESIPT process to provide the new tautomer keto (S_1-K) or return to the S_0-E state by emitting radiation. If the ESIPT process happens, the S_1-K keto tautomer reverts to the ground state *via* fluorescence emission to form S_0-K. Finally, the S_0-E enol form is recovered by ground state proton transfer (GSIPT). In addition, all five compounds are stable at the S_0-K state. Thus, it is predicted to exhibit a vertical transition to the Franck–Condon region S_1-K(FC). From this point, the molecules can regress to the S_1-K state with the structural rearrangement and then rapidly return to the ground state S_0-K by fluorescence emission.

The impact of polar and nonpolar solvents on the relative energy of the five molecules was investigated (Tables 2 and S1†). Similar to the gas phase, the keto structures in the three solvents at the S_0 state are less stable than the enol forms. The S_0-K form of **L1–L5** is more stable in the polar DMSO solvent than in the gas phase and other solvents by 3.34 to 5.01 (4 to 5.96 kcal mol^{-1}) by using the PBE0 (CAM-B3LYP) methods. From Table 2, the S_1-(FC) state of **L1–L5** has less energy in DMSO than in the gas phase and other solvents based on PBE0, indicating that these dyes are energetically

Table 2 Relative energies of **L1–L5** (R1–5 = –H, $–NH_2$, $–OCH_3$, $–CF_3$, and –CN) at the S_0 and S_1 states calculated at the PBE0/6-31++G(d,p) level

Media	Molecule	S_0-E	S_1(FC)	S_1-E	S_0-K	S_1-K
Gas	**L1**	0.00	69.04	61.10	7.46	66.60
	L2	0.00	69.64	64.04	6.14	66.51
	L3	0.00	69.58	63.05	5.63	66.92
	L4	0.00	66.43	57.29	6.87	62.41
	L5	0.00	63.89	55.10	7.03	60.46
DMSO	**L1**	0.00	65.71	57.88	5.01	59.05
	L2	0.00	66.28	58.27	3.65	60.07
	L3	0.00	66.42	58.60	3.34	59.19
	L4	0.00	63.10	55.42	4.40	56.42
	L5	0.00	59.98	52.79	4.57	54.14
MeOH	**L1**	0.00	66.03	57.97	5.05	59.17
	L2	0.00	66.64	58.38	3.69	60.19
	L3	0.00	66.74	58.69	3.37	59.31
	L4	0.00	63.40	55.55	4.43	56.54
	L5	0.00	60.27	52.86	4.61	54.27
Toluene	**L1**	0.00	66.07	60.57	6.33	63.20
	L2	0.00	66.64	61.86	5.03	64.35
	L3	0.00	66.71	61.65	4.57	63.34
	L4	0.00	63.39	57.43	5.72	60.54
	L5	0.00	60.54	55.02	5.87	58.46

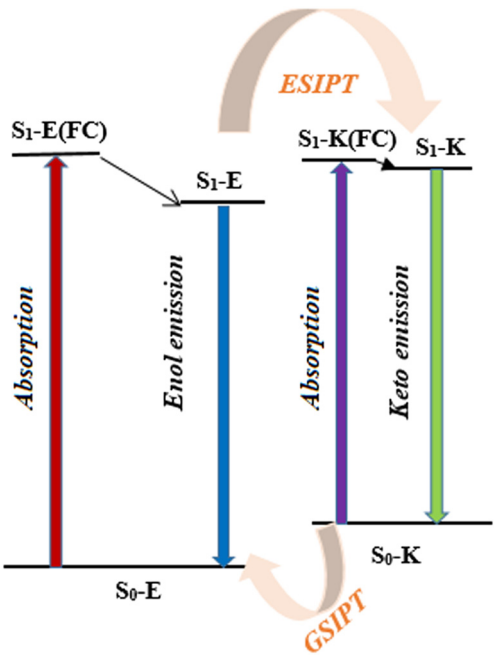

Fig. 3 The schematic representation of the ESIPT process involving enol–keto phototautomerization.

more stable in the polar DMSO solvent. The CAM-B3LYP energy difference between the S_1-E and S_1-(FC) states of the **L1–L5** (R1–5 = –H, $–NH_2$, $–OCH_3$, $–CF_3$, and –CN) azine-based dyes given in Table S1† is in the ranges of −10.67 to −15.38 in DMSO, −10.88 to −11.9 in MeOH and −6.98 to −7.29 kcal mol^{-1} in toluene, which are greater than the PBE0 ones. These values indicate that the conversion of the S_1-(FC) to S_1-E state in polar solvents is more exergonic than in the gas phase. The differences in energy between the two S_1-(FC) and S_1-K states are in the ranges of −5.84 to −7.23 kcal mol^{-1} (−8.87 to −14.68) in DMSO, −6.00 to −7.43 kcal mol^{-1} (−9.07 to −10.53) in MeOH and −2.08 to −3.37 kcal mol^{-1} (−4.68 to −6.02) in toluene based on the PBE0 (CAM-B3LYP) methods, indicating that the S_1-(FC) to S_1-K tautomerization in polar solvents is more exergonic than in the gas phase and the **L4** and **L5** dyes have the highest values.

3.3. The potential energy curves

To further investigate the influence of different substituents on the ESIPT process and elucidate the dynamics of ESIPT in the five studied molecules, the potential energy curves (PECs) along the proton transfer pathway as a function of the reaction coordinate (RC = d_{OH}) at the S_0 and S_1 states of the **L1–L5** molecules were computed at the PBE0/6-31++G(d,p) and TD-PBE0/6-31++G(d,p) levels of theory in the gas phase, respectively (Fig. 4). It can be seen that in the S_0 state, the enol (S_0-E) form is the most stable tautomeric form. As discussed previously, the molecular geometry optimization shows that the keto forms of all five molecules with O···H–N H-bonding are stable at the S_0 state. However, it can be seen that the O–H···N enol forms of **L1–L5** (R1–5 = –H, $–NH_2$, $–OCH_3$, $–CF_3$, and –CN) in the ground state are more stable

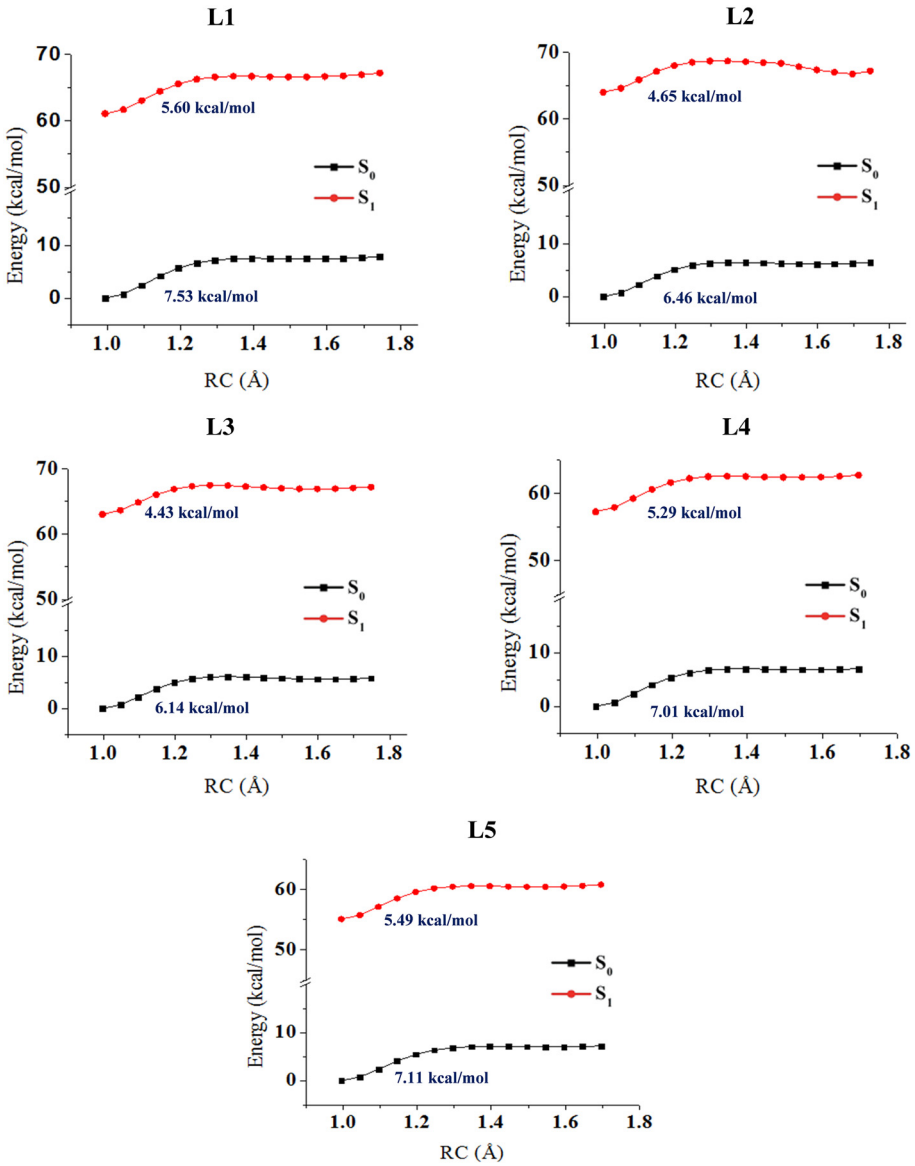

Fig. 4 The PBE0/6-31++G(d,p) PECs of **L1–L5** (R1–5 = –H, $–NH_2$, $–OCH_3$, $–CF_3$, and –CN) as functions of the reaction coordinate, RC (O–H), along the proton transfer at the S_0 and S_1 states.

than the corresponding O···H–N keto tautomers. From Fig. 4, the energy barrier at the S_0 state for enol → keto transformation in the **L1–L5** molecules is in the range of 6.14 to 7.53 kcal mol^{-1}. However, the energy barrier for the reverse process in **L1–L5** is 0.06, 0.30, 0.50, 0.13 and 0.08 kcal mol^{-1}, respectively, indicating that the keto → enol GSIPT is nearly a barrier-less process at the S_0 state. The potential energy curves show that the proton transfer energy barrier changes by adding substituents to the *meta* position of the OH group compared with the unsubstituted **L1**. In the excited state, the energy barrier is lower than the ground state, which indicates that the proton transfer is more facile in the S_1 state than in the S_0 one. The energy barrier order at the S_1 state is **L3** (4.43 kcal mol^{-1}) < **L2** (4.65 kcal mol^{-1}) < **L4** (5.29 kcal mol^{-1}) < **L5** (7.11 kcal mol^{-1}) < **L1** (5.60 kcal mol^{-1}). This trend implies that the energy barrier at the S_1 state for substituted molecules is smaller than the unsubstituted structure **L1** so the electron-donating groups facilitate the ESIPT process.

Most ESIPT molecules possess a strong H-bonding interaction, so ESIPT is either a barrier-less process or a small barrier one. The time scale for the ESIPT process is generally less than 1 ps, resulting in a lack of normal emission or weak normal emission, of course, there are exceptions.[68–71] The higher endergonic ESIPT can lead to weaker tautomer emission due to the lower population of the S_1-K keto species. In molecules in which the energy difference between S_1-E enol and S_1-K keto in the excited state and the corresponding barrier energies are small, an equilibrium between the two forms (reversible ESIPT) can be established before their respective emission.[72] The PECs and data given in Table 2 reveal that the S_1-K form of **L1–L5** (R1–5 = –H, $–NH_2$, $–OCH_3$, $–CF_3$, and –CN) is less stable than S_1-E by 5.5, 2.5, 3.9, 5.1 and 5.4 kcal mol^{-1}, respectively. Since the conversion of S_1-(FC) to S_1-E in **L1–L5** is an exergonic process by releasing the energy of −7.94, −5.60, −6.53, −9.14 and −8.79 kcal mol^{-1} based on PBE0, the formation of the keto tautomers is driven by the difference in energy between the S_1-(FC) and keto structures at the S_1 state. However, despite the reverse ESIPT being a barrier-less process, it is predicted that an equilibrium between the two enol and keto forms with the dominance of the enol form can be established before their corresponding emission. Accordingly, this process can affect the population of the enol and keto states and their respective contributions to the overall fluorescence and lead to changes in the relative intensities of the two bands and the emission characteristics of the system.

3.4. Vibrational spectra

Theoretical analysis of vibrational spectra is a well-established tool to assess the strength of H-bonding interactions. We reported the CAM-B3LYP results because the calculated O–H vibrational wavenumber for the **L1** dye (3338.1 cm^{-1}) was closer to the experimental result (3338.1 cm^{-1}) compared with PBE0 (3228.8 cm^{-1}). The CAM-B3LYP calculated vibrational spectra of azine derivatives **L1–L5** in the enol form at the S_0 state are given in Fig. S2.† The vibrational wavenumber of the O–H group involved in H-bonding can provide a specific measure of the H-bonding strength. The O–H vibrational wavenumber for **L1–L5** at the S_0-E state is 3338.05, 3292.33, 3283.35, 3314.87 and 3311.47 cm^{-1}, respectively, indicating that the O–H···N H-bonding strength is stronger in **L2** and **L3** with electron-donating substituents than in the other ones. There is a correlation between the O–H vibrational wavenumber and the O–H bond distance; the greater the O–H bond distance, the lower the corresponding vibrational wavenumber.

The vibrational spectra of keto tautomers with O···H–N H-bonding at the S_0 state are given in Fig. S3.† As can be seen, the intensity of the N–H band in the keto form is lower than the O–H one in the enol form. The N–H vibrational wavenumbers in the **L1–L5** dyes are 2927.40, 3012.01, 3060.07, 2947.25 and 2904.63 cm^{-1}, respectively. A comparison of O–H and N–H vibrational frequencies demonstrates that the O···H–N H-bonding in the keto form is stronger than the O–H···N one in the enol form, in good agreement with the corresponding H-bonding distances.

3.5. Photophysical properties

The photophysical characteristics of **L1–L5** (R1–5 = –H, $–NH_2$, $–OCH_3$, $–CF_3$, and –CN) including the absorption and emission wavelengths, oscillator strengths *f* and the vertical transition energies of the **L1–L5** molecules in the enol and keto forms calculated in the gas phase and three solvents at the PBE0/6-31++G(d,p) level are given in Tables 3 and 4 and those at the CAM-B3LYP/6-31++G(d,p) level are given in Tables S2 and S3.† As can be seen in Tables 3 and S2,† the calculated absorption wavelength (λ_1) for the S_0-E form of **L1** is 414 nm (351 nm) based on the PBE0 (CAM-B3LYP) methods. This reveals that the PBE0 wavelength for **L1** is closer to the experimental result (395 nm),[36] compared with the CAM-B3LYP one. The absorption wavelengths calculated for **L2**, **L3**, **L4** and **L5** are 410 (353), 410 (351), 430 (358) and 447 (364 nm) in the gas phase, suggesting that the absorption maxima are shifted to longer wavelengths by electron-withdrawing substituents. The first S_0 → S_1 vertical excitation energies (VEEs) of **L1** to **L5** are 2.99 (3.53), 3.02 (3.51), 3.02 (3.52) 2.88 (3.46) and 2.77 eV (3.40 eV), respectively. The PBE0 VEEs are smaller than the CAM-B3LYP ones, in good agreement with the reported results.[45,52]

The magnitude of the oscillator strength *f* for an electronic transition is proportional to the square of the transition dipole moment produced by the interaction between electromagnetic radiation and an electric dipole. The greater the transition dipole moment, the greater the transition probability between quantum states and in turn the greater the *f*. Thus, the intensity of the absorption peaks is proportional to the oscillator strength *f*. The PBE0 calculated oscillator strength *f* for the S_0 → S_1 vertical transition of the **L1–L5** (R1–5 = –H, $–NH_2$, $–OCH_3$, $–CF_3$, and –CN) molecules is in the order 1.493 (**L2**) > 1.395 (**L3**) > 1.195 (**L1**) > 1.158 (**L5**) > 1.155 (**L4**), and

Table 3 The calculated absorption and emission wavelengths (λ) and oscillator strength (f) of **L1**–**L5** (R1–5 = –H, –NH_2, –OCH_3, –CF_3, and –CN) in the gas phase at the PBE0/6-31++G(d,p) level

	S_0-E	S_1-E	S_0-K	S_1-K	S_0-E	S_1-E	S_0-K	S_1-K
	L1				**L2**			
λ_1 (nm)	414	545	452	558	410	505	434	563
λ_1 (eV)	2.99	2.27	2.74	2.22	3.02	2.45	2.85	2.2
λ_2 (nm)	339	390	391	468	336	392	388	458
λ_3 (nm)	337	387	371	402	332	377	356	423
f_1	1.195	0.138	1.064	0.213	1.493	0.311	1.261	0.209
f_2	0.076	0.769	0.123	0.356	0.167	1.213	0.222	1.211
f_3	0.001	0.008	0	0	0.018	0.001	0.001	0
	L3				**L4**			
λ_1 (nm)	410	519	437	528	430	599	461	616
λ_1 (eV)	3.02	2.39	2.83	2.34	2.88	2.07	2.69	2.01
λ_2 (nm)	334	390	377	446	342	395	393	456
λ_3 (nm)	331	378	353	382	336	386	371	403
f_1	1.395	0.222	1.299	0.344	1.155	0.102	1.172	0.121
f_2	0.166	1.167	0.064	0.385	0.002	0.003	0.017	0.533
f_3	0.002	0	0.0002	0	1.005	1.005	0	0
	L5							
λ_1 (nm)	447	626	474	645				
λ_1 (eV)	2.77	1.98	2.61	1.92				
λ_2 (nm)	348	400	402	458				
λ_3 (nm)	343	393	378	411				
f_1	1.158	0.107	1.176	0.118				
f_2	0.003	0.003	0.015	0.558				
f_3	0.295	1.207	0.0001	0				

Table 4 The calculated absorption and fluorescence emission properties of **L1**–**L5** (R1–5 = –H, –NH_2, –OCH_3, –CF_3, and –CN) in different solvents at the PBE0/6-31++G(d,p) level. The experimental values are given in parentheses

	S_0-E	S_1-E	S_0-K	S_1-K	S_0-E	S_1-E	S_0-K	S_1-K
DMSO	**L1**				**L2**			
λ_1 (nm)	435 (393)	578 (536)	471	606 (566)	431	534	450	545
f_1	1.357	1.53	1.307	1.533	1.73	2.07	1.602	1.855
MeOH								
λ_1 (nm)	432 (392)	535	468	565 (555)	429	534	448	544
f_1	1.332	1.518	1.284	1.526	1.7	2.061	1.572	1.847
Toluene								
λ_1 (nm)	432 (391)	514 (548)	471	534 (568)	429	495	451	513
f_1	1.376	0.891	1.294	1.259	1.723	1.676	1.572	1.521
DMSO	**L3**				**L4**			
λ_1 (nm)	430	531	456	549	453	562	488	589
f_1	1.558	1.817	1.499	1.723	1.301	1.387	1.288	1.437
MeOH								
λ_1 (nm)	428	530	453	548	450	560	485	588
f_1	1.532	1.808	1.476	1.717	1.277	1.376	1.267	1.428
Toluene								
λ_1 (nm)	428	498	456	517	451	557	485	563
f_1	1.577	1.37	1.509	1.457	1.428	0.598	1.323	0.985
DMSO	**L5**							
λ_1 (nm)	476	590	511	618				
f_1	1.288	1.461	1.26	1.415				
MeOH								
λ_1 (nm)	474	588	448	617				
f_1	1.263	1.444	1.572	1.406				
Toluene								
λ_1 (nm)	472	579	456	590				
f_1	1.322	0.682	1.509	0.918				

the CAM-B3LYP calculated order is 1.693 (**L2**) > 1.612 (**L3**) > 1.555 (**L5**) > 1.464 (**L4**) > 1.431 (**L1**), indicating that intensity of the $S_0 \rightarrow S_1$ transition peak for the **L2** and **L3** molecules with electron-donating groups is greater than that for the **L4** and **L5** molecules with electron-withdrawing substituents. As can be seen, the CAM-B3LYP calculated oscillator strengths are greater than the PBE0 ones.

There is an interpretation of longer wavelengths or lower VEEs observed for the **L4** and **L5** molecules compared to the other ones. Our results (see Fig. 6) show that the LUMO energy of **L4** and **L5** with the electron-withdrawing substituents CN and CF_3 decreases and that of **L2** and **L3** (R2 and 3 = NH_2 and OMe) increases relative to **L1** (R = H), leading to lower H–L energy gaps and longer wavelengths for them. It is clear that as the degree of electron delocalization increases, the energy gap between the HOMO and LUMO decreases, resulting in a shift in the electronic absorption spectrum towards longer wavelengths. To understand the effect of the substituents on the electron distribution in the phenyl ring, we used NBO analysis data. The results of NBO population analysis show that the oxygen lone pairs of the O–H group are mainly delocalized to vicinal anti-bonding orbitals BD*(C6–C4) and BD*(C6–C7), resulting in the decrease of LP population of the O atom (LP(O)). The average value of occupancy of LP(O) is 1.7932 in **L1**, 1.7942 in **L2**, 1.7938 in **L3**, 1.7921 in **L4** and 1.7923 in **L5**. This indicates that the delocalization of LP(O) towards BD* of the phenyl ring for **L4** and **L5** with electron-withdrawing substituents is greater than that for **L1**–**L3**. This is due to the inductive effect of the electron-withdrawing substituents which leads to the greater withdrawal of LP(O) electrons. This electron pull can increase the π-electron conjugation (electron density) of the phenol ring, thereby causing a bathochromic shift in absorption λ.[73,74] These LP(O) → BD*(C–C) charge transfer interactions increase the electron density on the phenyl ring and contribute to the π–π* interactions which shift the λ to longer wavelengths. The AIM results also show that the electron density at the ring critical point (RCP) of the phenol ring for **L2** (0.0203 au) and **L3** (0.0204 au) is lower than that for **L4** (0.0208 au) and **L5** (0.0206 au). The higher electron density and, in turn, the total electron energy density (H) in the RCP of the phenol ring suggest that the electrons are strongly delocalized in the center of the ring.[75]

After photoexcitation, the S_1-E form produced by relaxation of S_1-(FC) can either return to the S_0-E ground state *via* the fluorescence emission or is converted to the keto form through the ESIPT process. The PBE0 calculated S_1-E emission wavelengths (Table 3 and S2†) for **L1**–**L5** (R1–5 = –H, –NH_2, –OCH_3, –CF_3, and –CN) are 545 nm, 505, 519, 599 and 626 nm, respectively, which are longer than the CAM-B3LYP ones, similar to the absorption wavelengths. Moreover, all the molecules exhibit redshifted S_1-E emission relative to their vertical excitation wavelengths. The PBE0 Stokes shift for the S_1-E emission is in the order **L5** (179 nm) > **L4** (169 nm) > **L1** (131 nm) > **L3** (109 nm) > **L2** (95 nm). This indicates that the Stokes shift for the molecules with electron-withdrawing

substituents is smaller than the other ones. According to the oscillator strength f values given in Table 3, the trend of the intensity of S_1-E emission bands by using the PBE0 functional is **L2** (0.311) > **L3** (0.222) > **L1** (0.138) > **L5** (0.107) > **L4** (0.102) and that by using CAM-B3LYP is **L2** (1.823) > **L3** (1.749) > **L4** (1.691) > **L5** (1.574) > **L1** (1.563), indicating that the highest intensity of the S_1-E → S_0-E fluorescence emission corresponds to **L2** with the electron-donating $-NH_2$ group. As can be seen, the oscillator strength of the normal fluorescence emission calculated using the CAM-B3LYP functional is greater than the PBE0 one, similar to the absorption intensity.

The S_1-E form can be transformed into S_1-K through the ESIPT process and then return to the S_0-K state *via* fluorescence radiation emission. From Tables 3 and S2,† the calculated S_1-K fluorescence emission wavelengths for **L1**–**L5** (R1–5 = –H, $-NH_2$, $-OCH_3$, $-CF_3$, and –CN) by using the PBE0 (CAM-B3LYP) methods are 558 (451), 563 (432), 528 (433), 616 (450) and 645 nm (457 nm), respectively. These results reveal that the PBE0 emission wavelengths are greater than the CAM-B3LYP ones and the value for the **L1** dye is closer to the experimental value (566 nm). The calculated PBE0 Stokes shifts are higher than the CAM-B3LYP ones and follow the order: **L5** (198 nm) > **L4** (186 nm) > **L2** (153 nm) > **L1** > (144 nm) > **L3** (118 nm). Similar to enol emissions, the largest Stokes shifts are obtained for electron-withdrawing substituents. According to the results given in Table 3, the values of f for S_1-K → S_0-K transitions in **L1**–**L5** are in the ranges of 0.118–0.344 and 0.939–1.408 based on the PBE0 and CAM-B3LYP methods, respectively. It can be seen that except for **L2**, the PBE0 intensities of the S_1-K fluorescence emission bands are higher than those of S_1-E. The trend of the intensities of S_1-K emission bands is **L3** > **L1** > **L2** > **L4** > **L5** by the PBE0 method and **L3** > **L2** > **L5** > **L4** > **L1** by the CAM-B3LYP one, indicating that the highest intensity of the S_1-K fluorescence emission corresponds to **L3** with the electron-donating $-OCH_3$ group.

The effect of solvents on the absorption and emission peaks of the studied molecules was explored. The solvents with different dielectric constants namely dimethylsulfoxide (DMSO: ε = 46.826), methanol (MeOH: ε = 32.613) and toluene (ε = 2.3741) were selected and the results are listed in Tables 4 and S3.† The PBE0 calculated absorption and

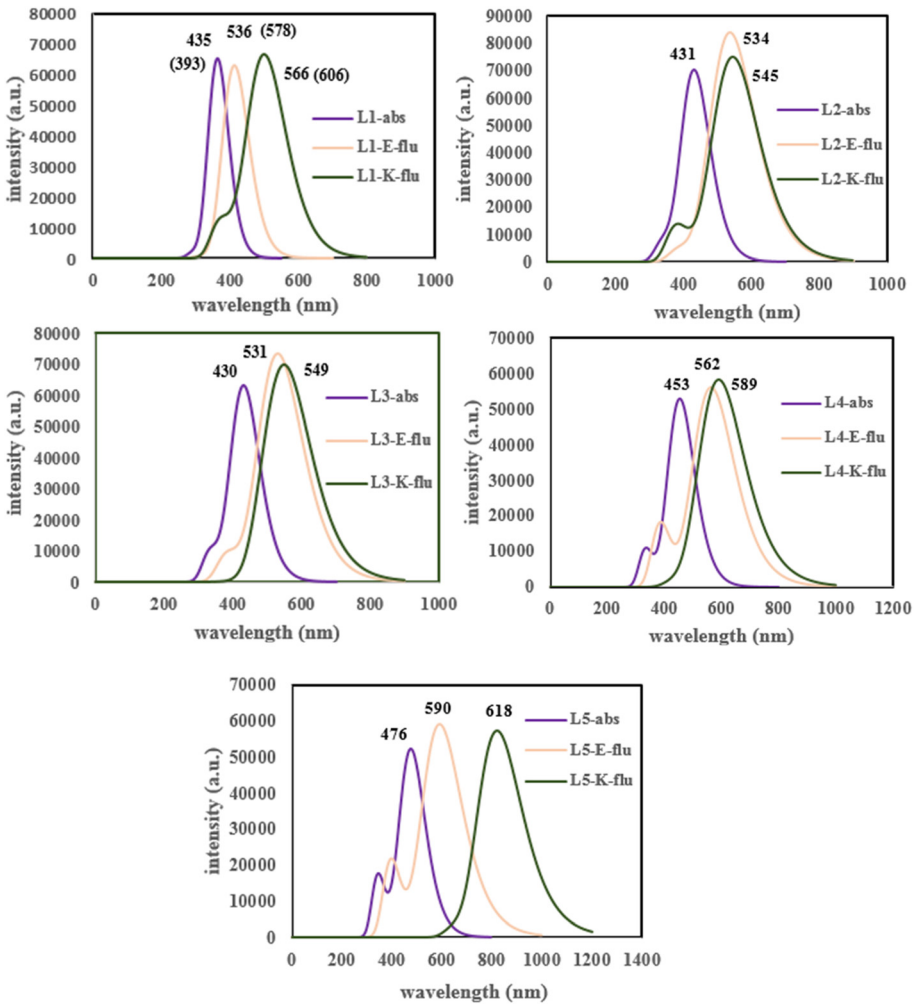

Fig. 5 The absorption and emission spectra of **L1**–**L5** (R1–5 = –H, $-NH_2$, $-OCH_3$, $-CF_3$, and –CN) in DMSO solvent at the PBE0/6-31++G(d,p) level. The values in parentheses are experimental data (abs = absorption spectrum; flu = fluorescence spectrum).

emission spectra in DMSO solvent are shown in Fig. 5. The corresponding spectra in MeOH and toluene solvents are shown in Fig. S4 and S5 of the ESI.† The highest absorption wavelengths calculated for **L1–L5** in the three solvents by using the PBE0 (CAM-B3LYP) methods are in the ranges of 432 to 435 nm (362 to 363 nm) for **L1**, 429 to 431 nm (365 to 367 nm) for **L2**, 428 to 430 nm (362 to 364 nm) for **L3**, 450 to 453 nm (368 to 370 nm) for **L4** and 472 to 476 nm (376 to 378 nm) for **L5**. The PBE0 (CAM-B3LYP) calculated absorption wavelength for **L1** is 435 nm (363 nm) in DMSO and 432 nm (362 nm) in MeOH and toluene. Compared with the experimental results given for **L1**, the PBE0 functional overestimates the absorption wavelengths in all solvents and the CAM-B3LYP functional underestimates them. However, both CAM-B3LYP and PBE0 values for **L1** are close to the experimental values (393 nm in DMSO, 392 nm in MeOH and 391 nm in toluene).[36] It can be seen that the bathochromic shift in the absorption wavelength values for **L4** and **L5** is greater than those for **L1**, **L2** and **L3**. The CAM-B3LYP oscillator strengths f for the $S_0 \rightarrow S_1$ vertical transition are greater than the PBE0 ones and in DMSO, MeOH and toluene follow the order: **L2** > **L3** > **L5** > **L4** > **L1**.

The calculated enol S_1-E emission wavelengths for **L1–L5** in solvent media are in the ranges of 514–536 nm (443–481 nm) for **L1**, 495–534 nm (450–492 nm) for **L2**, 498–531 nm (446–484 nm) for **L3**, 557–562 nm (452–493 nm) for **L4** and 579–590 nm (465–512 nm) for **L5** based on the PBE0 (CAM-B3LYP) functionals. From Tables 4 and S3,† a slight red shift can be observed in enol emission for all the molecules with an increase in the polarity of the solvent, in good agreement with the bathochromic shift observed by an increase in the polarity of the solvent.[36] In addition, the enol emission wavelengths of the S_1-E form for **L1** are 536 nm (481) in DMSO, 535 nm (480 nm) in MeOH and 514 nm (443 nm) in toluene. The PBE0 calculated values are closer to the experimental values (578 nm in DMSO and 548 nm in toluene).[36] Compared with the experimental results given for **L1**, the PBE0 functional overestimates the emission wavelengths in all solvents and the CAM-B3LYP functional underestimates them and both functionals underestimate the enol emission wavelength in toluene solvent.

The PBE0 (CAM-B3LYP) calculated S_1-K fluorescence emission bands of **L1–L5** in the three solvents are in the ranges of 534–566 nm (470–500 nm) for **L1**, 513–545 nm (458–490 nm) for **L2**, 517–549 nm (459–490 nm) for **L3**, 563–589 nm (477–512 nm) for **L4** and 590–618 nm (488–526 nm) for **L5**. The calculated keto emission of the S_1-K state for **L1** appears at 566 nm (500 nm) in DMSO, 565 nm (499 nm) in MeOH and 534 nm (470 nm) in toluene by using the PBE0 (CAM-B3LYP) methods. These results are well comparative with the experimental data (606 nm in DMSO, 555 nm in MeOH and 568 nm in toluene).[36] However, the PBE0 results are closer to the experimental values available for **L1**. In addition, the largest PBE0 Stokes shifts computed in MeOH solvent follow the order 143 nm (**L5**) > 138 (**L4**) > 133 (**L1**) > 120 (**L3**) > 115 (**L2**). It can be concluded that the Stokes shifts for **L4** and **L5** containing electron-withdrawing groups are greater than those for **L2** and **L3** possessing electron-donating substituents. According to the f values given in Tables 4 and S3,† the intensities of S_1-K and S_1-E fluorescence emission bands in solvent media are higher than those in the gas phase.

The dipole moments for azine derivatives **L1–L5** (R1–5 = –H, $–NH_2$, $–OCH_3$, $–CF_3$, and –CN) in the gas phase and solvent media are listed in Table 5. The change in dipole moment upon photoexcitation is associated with the reorganization of the electron density and the redistribution of charges within the molecule through intramolecular charge transfer (ICT). The strength of the push–pull substituents can affect the charge distribution and, consequently, the molecular dipole moment and their photophysical properties in solvent media. The charge separation is proportional to the electron-donating/withdrawing strength. It should be noted that $–NH_2$ is a better push group than –OMe because of the lower electronegativity of the nitrogen atom; at the same time, the –CN substituent pulls electrons more than $–CF_3$. According to the PBE0 results, in the gas phase, the ground-state dipole moment values range from 1.3 to 10.2 D and 2.7 to 12.3 D for the enol and keto forms, respectively, which (except for **L2**) decrease upon the S_0 to S_1 transition. The different behavior of the **L2** molecule can be attributed to the lower value of RMSD (4.95) upon the S_0 to S_1 transition, compared with the other molecules (5.2 to 37.8). The dipole moment values are in the range of 1.0 to 5.9 D in the S_1-E form and 0.8 to 7.5 D in the S_1-K form. The differences between the ground and excited state dipole moments in the **L4** and **L5** dyes with electron-withdrawing substituents are higher than the other ones. In addition, **L4** and **L5** exhibit larger dipole moment changes than the other ones upon enol to keto tautomerization in the S_1 state.

The change in dipole moment upon photoexcitation can provide valuable information about the solvatochromic effect. The PBE0 dipole moment values (Table 5) at the S_0-E state range from 1.6 D for **L2** to 12.5 D for **L5** in the protic CH_3OH polar solvent, 1.6 D for **L2** to 12.6 D for **L5** in the aprotic DMSO polar solvent and 1.5 D for **L2** to 11.5 D for **L5** in the

Table 5 The PBE0 calculated dipole moments (Debye) of the azine dyes **L1–L5** (R1–5 = –H, $–NH_2$, $–OCH_3$, $–CF_3$, and –CN)

	S_0-E	S_1-E	S_0-K	S_1-K	S_0-E	S_1-E	S_0-K	S_1-K
	Gas				DMSO			
L1	3.6	1.0	5.6	2.3	4.9	4.2	8.3	7.9
L2	1.3	3.2	2.7	4.0	1.6	1.7	4.1	4.1
L3	1.8	1.5	3.8	0.8	2.9	2.4	6.0	5.8
L4	7.9	4.3	10.0	5.9	9.7	9.1	13.1	12.5
L5	10.2	5.9	12.3	7.5	12.6	11.9	16.1	15.1
	MeOH				Toluene			
L1	4.9	4.1	8.2	7.9	4.3	2.1	6.9	6.2
L2	1.6	1.7	4.1	4.0	1.5	1.9	3.3	3.2
L3	2.9	2.3	6.0	5.7	2.3	0.9	4.8	4.1
L4	9.6	8.9	13.1	12.4	8.8	6.1	11.6	9.3
L5	12.5	11.8	16.0	15.0	11.5	8.4	14.2	11.3

nonpolar toluene solvent, indicating that the dipole moment slightly decreases going from the polar solvent to the nonpolar one. From the small changes of the dipole moment with the change of solvent, it is predicted that the absorption wavelength does not significantly change when the polarity of the solvent changes, as the results of Table 4 show (weak solvatochromism in the absorption band).

The PBE0 dipole moment values at the S_1-E state are in the range of 1.7 D for **L2** to 11.8 D for **L5** in CH_3OH, 1.7 D for **L2** to 11.9 D for **L5** in DMSO and 0.9 D for **L3** to 8.4 D for **L5** in the toluene solvent, indicating that the dipole moment slightly decreases going from the polar solvent to the nonpolar one at the S_1-E state. The small increase in the dipole moment of the enol form (except for **L2**) going from S_1-E to S_0-E in the polar solvents DMSO and CH_3OH is consistent with the results of the small solvation effect for the emission bands of the enol form. However, the increase in dipole moment for the enol form upon the S_1-E to S_0-E transition in toluene is greater than that in the polar solvents, which results in the shorter enol emission wavelength in toluene, as given in Table 4. The increase in dipole moment for the **L4** and **L5** molecules in toluene is greater than the other ones.

For keto forms, the dipole moment increases in all solvents upon the S_1-K to S_0-K transition so its value in the toluene solvent is greater than the other ones. Therefore, a decrease in solvent polarity is conducive to stabilizing the S_0-K state due to a larger increase in dipole moment. Accordingly, a red shift in keto fluorescence emission (positive solvatochromic effect) is estimated by an increase in the polarity of the solvent, as can be seen in Table 4 (458–488 nm in toluene and 489–525 nm in polar solvents), in good agreement with results given in ref. 36. In addition, an increase in dipole moment in the three solvents is found upon enol to keto switching through the ESIPT process in the S_1 state, showing that the keto form is more stabilized than the enol form and can emit in longer wavelength.

Based on the results given in Tables 6 and 7, the $S_0 \rightarrow S_1$ and $S_1 \rightarrow S_0$ transitions in **L1** to **L5** are mainly described as HOMO (H) → LUMO (L) and LUMO (L) → HOMO (H) transitions, respectively, with more than 69% contribution, demonstrating that the HOMO–LUMO contribution is dominant. Accordingly, the calculated highest occupied molecular orbitals (HOMOs) and lowest occupied molecular orbitals (LUMOs) for the enol and keto forms of **L1**–**L5** in the gas phase are presented in Fig. 6. It can be seen that the first transition to the excited state has a ππ* feature due to the π character of the HOMO as well as the π* character of the LUMO. The electron density in the HOMO of all molecules at the S_0-E state is distributed on the whole of the molecule including the triphenylamine (donor), azine and phenol units, and that in the LUMO is located mainly on the azine and substituted phenol units. A comparison of the electron density distribution of the HOMO and LUMO reveals that intramolecular charge transfer (ICT) occurs from triphenylamine to salicylaldimine (phenol-C═NH) as an acceptor unit upon excitation from S_0 to S_1. This ICT process can facilitate the proton transfer.

Table 6 The calculated absorption properties of **L1**–**L5** (R1–5 = –H, $–NH_2$, $–OCH_3$, $–CF_3$, and –CN) at the PBE0/6-31++G(d,p) level of theory

	Media	Transition	E (eV)	λ_{abs} (nm)	f	Component	CI (%)
L1	Gas	$S_0 \rightarrow S_1$	2.99	414	1.195	H → L	69.84
		$S_0 \rightarrow S_2$	3.65	339	0.076	H-1 → L	67.71
		$S_0 \rightarrow S_3$	3.68	337	0.001	H-2 → L	68.64
	DMSO	$S_0 \rightarrow S_1$	2.85	435	1.357	H → L	69.77
	MeOH		2.86	432	1.332	H → L	69.81
	Toluene		2.87	432	1.375	H → L	69.69
L2	Gas	$S_0 \rightarrow S_1$	3.02	410	1.493	H → L	69.86
		$S_0 \rightarrow S_2$	3.68	336	0.167	H-1 → L	67.98
		$S_0 \rightarrow S_3$	3.73	332	0.017	H → L + 1	66.34
	DMSO	$S_0 \rightarrow S_1$	2.87	431	1.73	H → L	69.93
	MeOH		2.89	429	1.7	H → L	69.94
	Toluene		2.89	429	1.723	H → L	69.89
L3	Gas	$S_0 \rightarrow S_1$	3.02	411	1.395	H → L	69.89
		$S_0 \rightarrow S_2$	3.7	334	0.165	H-1 → L	67.77
		$S_0 \rightarrow S_3$	3.73	331	0.002	H-3 → L	68.65
	DMSO	$S_0 \rightarrow S_1$	2.88	430	1.557	H → L	69.8
	MeOH		2.89	428	1.532	H → L	69.83
	Toluene		2.89	428	1.577	H → L	69.77
L4	Gas	$S_0 \rightarrow S_1$	2.88	430	1.155	H → L	69.98
		$S_0 \rightarrow S_2$	3.62	342	0.002	H-3 → L	69.55
		$S_0 \rightarrow S_3$	3.68	336	0.183	H-1 → L	67.46
	DMSO	$S_0 \rightarrow S_1$	2.75	450	1.277	H → L	69.9
	MeOH		2.74	453	1.301	H → L	69.86
	Toluene		2.75	451	1.318	H → L	69.86
L5	Gas	$S_0 \rightarrow S_1$	2.77	447	1.157	H → L	70.06
		$S_0 \rightarrow S_2$	3.56	348	0.002	H-3 → L	69.26
		$S_0 \rightarrow S_3$	3.61	343	0.294	H-1 → L	65.15
	DMSO	$S_0 \rightarrow S_1$	1.29	476	1.288	H → L	69.88
	MeOH		2.61	474	1.262	H → L	69.93
	Toluene		2.62	472	1.322	H → L	69.77

The HOMO–LUMO (H–L) energy gap for **L1** to **L5** at the S_0-E state follows the order **L2** and **L3** (3.54 eV) > **L1** (3.49 eV) > **L4** (3.35 eV) > **L5** (3.21 eV), in good agreement with the lower excitation energy or greater absorption wavelength calculated for **L4** and **L5** having electron-withdrawing substituents. The simultaneous destabilization of the π HOMO by the electron-donating substituent and stabilization of the π* LUMO by the electron-withdrawing substituent in **L4** and **L5** result in the decrease of the H–L gap and, in turn, the red shift of the ππ* absorption.

As Fig. 6 shows, the electron density in the LUMO of the S_1-E state is mainly distributed on the azine and substituted phenol units and that in the HOMO is located in the triphenylamine donor group. This indicates that the ICT process takes place upon enol emission. The H–L energy gap for **L1**–**L5** at the S_1-E state is 2.86, 3.03, 2.98, 2.61 and 2.48 eV respectively, which are in good agreement with the corresponding normal emission wavelengths.

The (H–L) energy gaps of keto tautomers at the S_1-K state for **L1** (2.77), **L2** (2.79), **L3** (2.90), **L4** (2.53) and **L5** (2.41 eV) are smaller than those of their enol structures, which are **L1** (2.86), **L2** (3.03), **L3** (2.98) **L4** (2.61) and **L5** (2.48 eV) at the S_1-E state, indicating that the keto forms of these molecules will emit longer fluorescence emission wavelengths. Moreover,

Table 7 The calculated fluorescence properties and composition index (CI) of molecular orbitals involved in transitions in the enol and keto (given in parentheses) forms of **L1**–**L5** (R1–5 = –H, $–NH_2$, $–OCH_3$, $–CF_3$, and –CN) at the PBE0/6-31++G(d,p) level

	Media	Transition	E_{flu} (eV)	λ_{flu} (nm)	f	Component	CI (%)
L1	Gas	$S_1 \rightarrow S_0$	2.27 (2.22)	545 (558)	0.138 (0.213)	L → H (L → H)	69.90 (69.84)
	DMSO	$S_1 \rightarrow S_0$	2.31 (2.18)	535 (566)	1.530 (1.533)	L → H (L → H)	69.86 (69.42)
	MeOH	$S_1 \rightarrow S_0$	2.32 (2.19)	535 (565)	1.518 (1.526)	L → H (L → H)	69.86 (69.43)
	Toluene	$S_1 \rightarrow S_0$	2.41 (2.32)	514 (534)	0.891 (1.259)	L → H (L → H)	69.99 (69.89)
L2	Gas	$S_1 \rightarrow S_0$	2.45 (2.20)	505 (563)	0.311 (0.209)	L → H (L → H)	69.72 (69.48)
	DMSO	$S_1 \rightarrow S_0$	2.31 (2.27)	536 (545)	2.070 (1.855)	L → H (L → H)	70.19 (69.80)
	MeOH	$S_1 \rightarrow S_0$	2.32 (2.28)	534 (544)	2.061 (1.847)	L → H (L → H)	70.19 (69.80)
	Toluene	$S_1 \rightarrow S_0$	2.50 (2.42)	495 (513)	1.676 (1.521)	L → H (L → H)	70.13 (69.87)
L3	Gas	$S_1 \rightarrow S_0$	2.39 (2.34)	519 (528)	0.222 (0.344)	L → H (L → H)	69.87 (69.77)
	DMSO	$S_1 \rightarrow S_0$	2.33 (2.26)	531 (549)	1.817 (1.723)	L → H (L → H)	70.02 (69.68)
	MeOH	$S_1 \rightarrow S_0$	2.34 (2.26)	530 (548)	1.808 (1.717)	L → H (L → H)	70.03 (69.69)
	Toluene	$S_1 \rightarrow S_0$	2.49 (2.40)	498 (517)	1.370 (1.457)	L → H (L → H)	70.09 (69.98)
L4	Gas	$S_1 \rightarrow S_0$	2.07 (2.01)	599 (616)	0.102 (0.121)	L → H (L → H)	69.90 (69.88)
	DMSO	$S_1 \rightarrow S_0$	2.21 (2.10)	562 (589)	1.387 (1.437)	L → H (L → H)	69.79 (69.29)
	MeOH	$S_1 \rightarrow S_0$	2.21 (2.11)	560 (588)	1.376 (1.428)	L → H (L → H)	69.80 (69.30)
	Toluene	$S_1 \rightarrow S_0$	2.22 (2.20)	557 (563)	0.598 (0.985)	L → H (L → H)	69.97 (69.76)
L5	Gas	$S_1 \rightarrow S_0$	1.98 (1.92)	626 (645)	0.107 (0.118)	L → H (L → H)	69.87 (69.90)
	DMSO	$S_1 \rightarrow S_0$	2.10 (2.00)	590 (618)	1.461 (1.415)	L → H (L → H)	69.71 (69.27)
	MeOH	$S_1 \rightarrow S_0$	2.11 (2.01)	588 (617)	1.444 (1.406)	L → H (L → H)	69.72 (69.28)
	Toluene	$S_1 \rightarrow S_0$	2.14 (2.10)	579 (590)	0.682 (0.918)	L → H (L → H)	69.97 (69.81)

the transition properties involving the electronic excitation energy, corresponding oscillator strengths (f) and composition index for absorption transitions in the gas phase and solvent media are summarized in Table 6 and the fluorescence properties are listed in Table 7. It can be seen that **L1**–**L5** show absorption maxima in the ranges of 410 to 447 nm (f = 1.155 to 1.493) which are mainly due to the HOMO (H) → LUMO (L) transition with the largest contributions in the ranges of 69.84 to 70.06% in the gas phase. The $S_0 \rightarrow S_2$ transition which involves HOMO-1 (H-1) → LUMO (L) for **L1**, **L2**, and **L3** and HOMO-3 (H-3) → LUMO (L) for **L4** and **L5** is also allowed, and despite the large orbital contributions, their oscillator strengths are in the ranges of 0.002 to 0.167. Thus, it is predicted that $S_0 \rightarrow S_1$ is the main light transition in these compounds. In solution, we mainly focus on the $S_0 \rightarrow S_1$ transition. Thus, it can be seen that in DMSO, MeOH and toluene media, the HOMO (H) → LUMO (L) transition contributes more than 69% for **L1** to **L5**. According to the results given in Table 7, the $S_1 \rightarrow S_0$ enol and keto emissions of **L1** to **L5** are related to LUMO (L) → HOMO (H) transitions with more than 69% contribution in the gas phase and solvent media.

The fluorescence rate constants, k_f, are calculated for the S_1-E and S_1-K forms of **L1**–**L5** (R1–5 = –H, $–NH_2$, $–OCH_3$, $–CF_3$, and –CN) *via* Einstein's emission transition probability equation: $k_f = \frac{f \times [\nu\ (\mathrm{cm}^{-1})]^2}{1.5}$ (ref. 76), where ν is the fluorescence wavenumber and f is the oscillator strength. The calculated fluorescence rate constants, k_f, and fluorescence lifetimes ($\tau = 1/k_f$) in the gas phase and solvent media are reported in Table 8. For **L1**–**L5**, the fluorescence lifetime of the S_1-E state follows the order: **L5** > **L4** > **L1** > **L3** > **L2**. The most significant effect of electron-withdrawing substitutions in **L4** and **L5** is the smaller k_f and, in turn, the longer ππ* lifetime (τ_f) compared with the other molecules in the gas phase and all solvent media, where the S_1-E state in **L4** and **L5** has a lifetime three times longer than that in **L2** and **L3** in the gas phase and toluene solvent, although the lifetime of the S_1-E state of **L4** and **L5** is greater than that of **L2** and **L3** in the polar solvent. The results show that the lifetime of the S_1-E state in all molecules is nearly the same in polar solvents and is longer in toluene solvent than in the polar ones.

Similar to the S_1-E state, the lifetime of the S_1-K state for **L4** and **L5** in all media is greater than that found in **L2** and **L3**, indicating that **L4** and **L5** containing electron-withdrawing groups have longer lifetimes compared with **L2** and **L3** having electron-donating substituents. The comparison of rate constants for the studied molecules reveals that the emission rate constants of the S_1-E form for **L1**, **L4** and **L5** are smaller than those of S_1-K in the gas phase and toluene and it is the opposite for **L2** and **L3**. In the polar solvent media, there is no particular order.

3.6. Hole–electron excitation properties

After photoexcitation, electron transfer occurs from the donor group (D) to the acceptor (A). In the studied molecules, the excitation mainly occurs from the HOMO to the LUMO. However, the substituent effects on ICT degrees cannot be quantitatively given *via* HOMO and LUMO isosurfaces. Furthermore, orbital analysis may be difficult to be directly connected to simple chemical parameters and concepts such as the charge transfer extent. To solve this problem, several approaches have been derived to analyze the character of the excited states, specifically, to quantify the degree of locality and nonlocality of an excitation, meaning by computing the hole–electron properties upon photoexcitation. Herein, the "hole" signifies the region where the excited electron leaves,

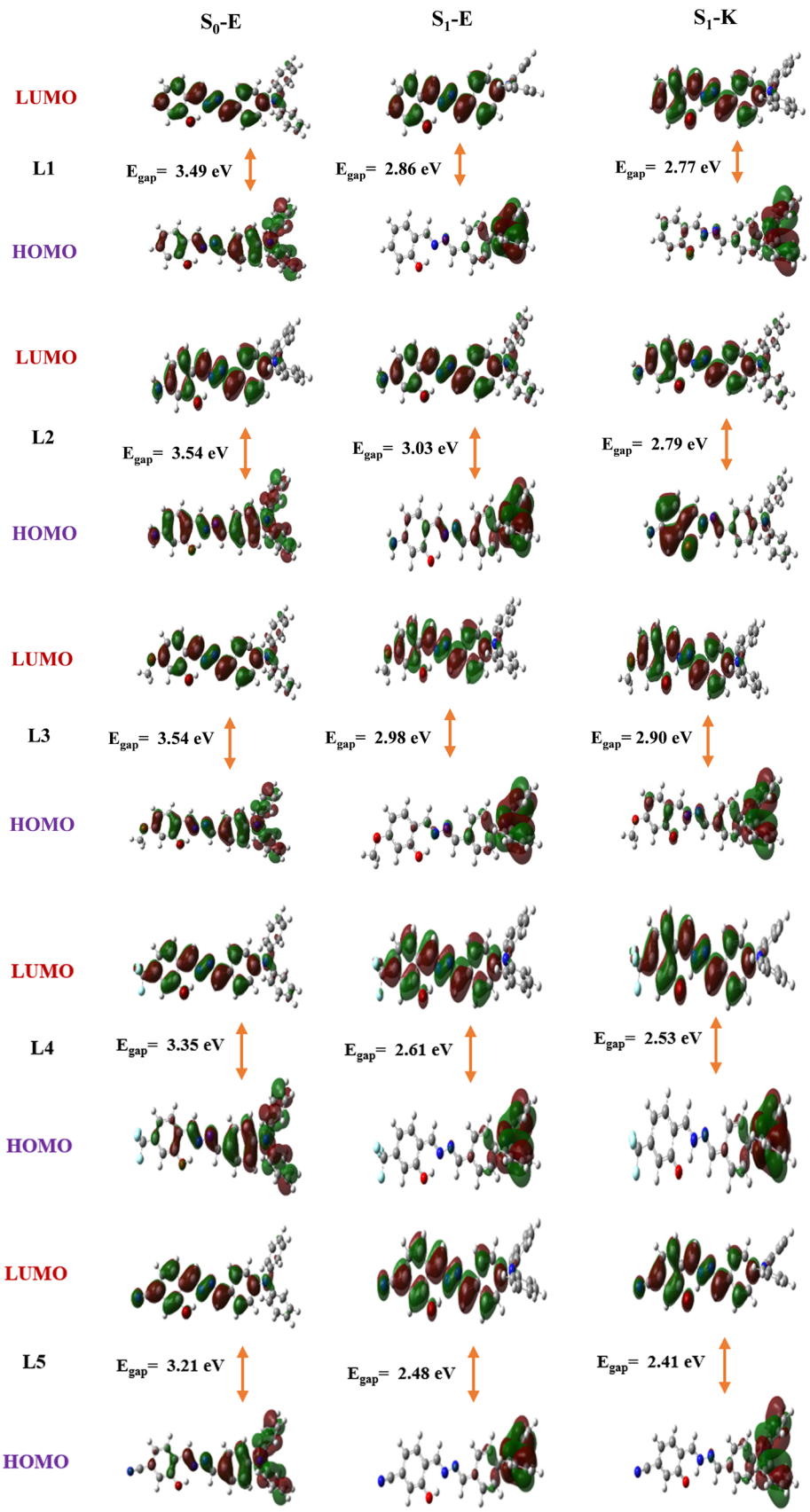

Fig. 6 Isodensity surface plots of the HOMOs and LUMOs of **L1**–**L5** (R1–5 = –H, $–NH_2$, $–OCH_3$, $–CF_3$, and –CN) involved in the first singlet excitation calculated at the PBE0/6-31++G(d,p) level. The numerical values are the HOMO–LUMO energy gap. Isosurfaces are set to 0.02.

Table 8 The S_1-E and S_1-K fluorescence rate constants (k_f) and radiation lifetimes (τ_f) for **L1–L5** (R1–5 = –H, $–NH_2$, $–OCH_3$, $–CF_3$, and –CN) calculated at the PBE0/6-31++G(d,p) level

		S_1-E		S_1-K	
Media	Molecule	k_f (s^{-1})/10^6	τ_f (ns)	k_f (s^{-1})/10^6	τ_f (ns)
Gas	**L1**	30.94	32.32	45.41	22.02
	L2	81.10	12.33	43.90	22.77
	L3	54.82	18.24	81.96	12.20
	L4	18.87	52.94	21.27	47.01
	L5	18.09	55.27	18.88	52.96
DMSO	**L1**	354.31	2.82	318.17	3.14
	L2	479.59	2.08	415.19	2.40
	L3	428.81	2.32	415.07	2.41
	L4	292.53	3.41	275.99	3.62
	L5	279.88	3.57	348.53	2.86
MeOH	**L1**	352.86	2.83	476.89	2.09
	L2	480.10	2.08	415.07	2.40
	L3	428.57	2.33	380.24	2.62
	L4	292.25	3.42	275.38	3.63
	L5	277.58	3.60	245.84	4.06
Toluene	**L1**	224.75	4.45	293.79	3.41
	L2	454.6	2.19	385.13	2.60
	L3	367.2	2.72	363.22	2.75
	L4	128.28	7.79	207.00	4.83
	L5	135.46	7.38	175.71	5.69

and the "electron" is the region where the excited electron eventually goes.[65]

The hole–electron excitation descriptors including the charge transfer (CT) excitation distance (D_{CT}), transferred charge (q_{CT}), variation in dipole moment between the ground and excited states (μ_{CT}), H_{CT} (Å), H index (Å), t index (Å) and overlap integral between ρ_- and ρ_+ regions ($S_\pm$) computed at the PBE0/6-31++G(d,p) level for **L1–L5** in the gas phase and DMSO solvent are given in Table 9.

The process of single-electron excitation involves an electron moving from a hole to an electron. The simultaneous distribution of holes and electrons on the dyes is illustrated in Fig. 7. The green isosurface represents the electron distribution, and the blue isosurface represents the hole distribution; the isovalue has been set to 0.002. This indicates that the hole isosurface of these dyes is mainly distributed over the electron-donating part, TPA, and the electron delocalized mainly over the acceptor moiety. The separated distribution of holes and electrons leads to the electron movement from the donor group to the acceptor one. In **L2** and **L3** with electron-withdrawing substituents, the holes are also extended to the substituents, leading to a decrease in CT. From the distribution of holes and electrons, we can infer that the hole and electron distributions should be composed of π and π* orbitals, respectively. Therefore, it can be concluded that $S_0 \rightarrow S_1$ is a CT excitation with a π → π* feature. If an excitation is perfectly described as a HOMO → LUMO transition, then the hole and electron could be simply represented by the HOMO and LUMO, respectively, as can be observed for the $S_0 \rightarrow S_1$ transition in these dyes.

The widespread application of the D_{CT} index in a wide range of very different molecular systems is due to its simplicity, effectiveness, and straightforward interpretation. The calculation of the D_{CT} index requires only the calculation of the electronic density of the ground (ρ^{GS}) and excited (ρ^{ES}) states of interest. The density change associated with the electronic transition is given by $\Delta\rho(r) = \rho^{ES} - \rho^{GS}$. From $\Delta\rho(r)$, the first two ρ_+ and ρ_- functions are defined which show the points in space where an increment or a depletion of the electron density occurs upon excitation. Then, from these two ρ_+ and ρ_- charge distribution functions, D_{CT} can be expressed as the spatial distance between the two barycenters of the positive (R_+) and negative (R_-) density distributions: $D_{CT} = |R_+ - R_-|$. D_{CT} has a vectorial character which is the difference between the positions of the two barycenters. This descriptor can be used as a measure of the effective distance of the electron and the hole upon excitation.[65,77]

From Table 9, the D_{CT} for **L2** (2.857 Å) and **L3** (3.385 Å) having the electron-donor groups NH_2 and OMe is lower than that for **L1** (3.996 Å) and the D_{CT} for **L4** (4.549 Å) and **L5** (5.075 Å) having the electron acceptor groups CF_3 and CN is greater than that for **L1**. Therefore, the distance between the hole and electron centroids (charge transfer length) in **L4** and **L5** is greater than the other ones. Nevertheless, the D_{CT} values are relatively high, indicating that there is a significant separation of the hole and electron distributions. Therefore, the $S_0 \rightarrow S_1$ transition in the **L1–L5** compounds is attributed to CT excitation rather than locally excited (the D_{CT} value is small), in good agreement with the predictions based on HOMO and LUMO isosurfaces.

The transferred charge (q_{CT}) can be obtained by integrating over all space ρ_+ and ρ_-. For one electron

Table 9 Computed CT indices for vertical transition of **L1–L5** (R1–5 = –H, $–NH_2$, $–OCH_3$, $–CF_3$, and –CN) calculated at the PBE0/6-31++G(d,p) level in the gas and DMSO media

	D_{CT}/Å	q_{CT}/|e|	$\|\mu_{CT}\|$/Debye	H_{CT}/Å	H index/Å	t index/Å	$S_\pm$ index
L1 (gas)	3.996	0.643	12.337	4.218	4.694	−0.222	0.858
L1 (DMSO)	4.862	0.708	16.53	4.123	4.603	0.739	0.808
L2 (gas)	2.857	0.56	7.681	4.292	4.713	−1.435	0.917
L2 (DMSO)	2.858	0.596	8.185	4.287	4.68	−1.430	0.911
L3 (gas)	3.385	0.593	9.634	4.311	4.755	−0.926	0.896
L3 (DMSO)	4.073	0.649	12.700	4.132	4.587	−0.059	0.857
L4 (gas)	4.549	0.71	15.517	4.479	4.936	0.070	0.843
L4 (DMSO)	5.454	0.769	20.144	4.339	4.809	1.115	0.791
L5 (gas)	5.075	0.746	18.178	4.624	5.071	0.451	0.820
L5 (DMSO)	6.18	0.811	24.100	4.552	5.004	1.628	0.762

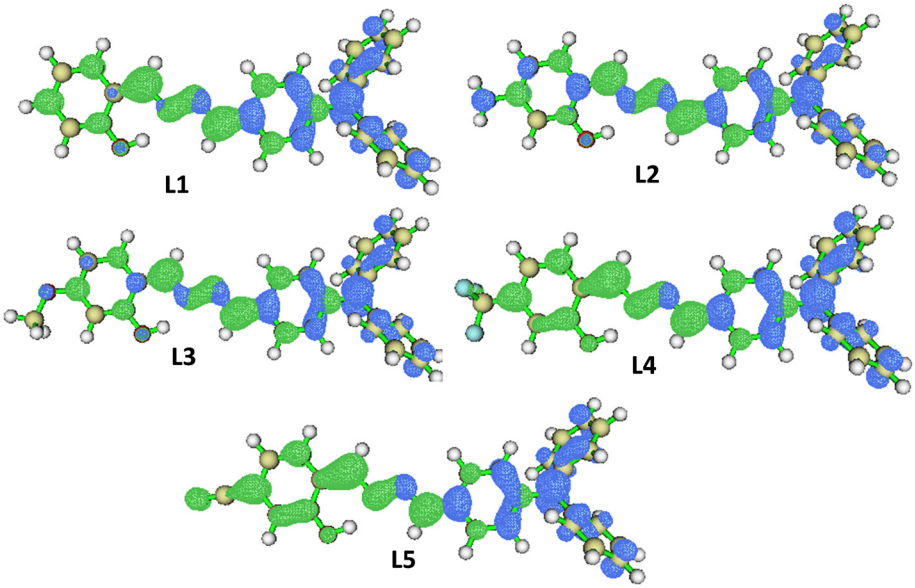

Fig. 7 The simultaneous distribution of hole and electron isosurfaces on the **L1**–**L5** dyes calculated at the PBE0/6-31++G(d,p) level in the gas phase. The isovalue has been set to 0.002. The blue and green isosurfaces are related to the hole and electron distributions, respectively.

excitation, q_{CT} can receive values between 0 and 1.[65] In agreement with D_{CT}, the transferred charge, q_{CT}, value increases as the substituents vary from the electron-donating group to the electron-withdrawing group. For one electron excitation, q_{CT} can assume values between 0 and 1. The q_{CT} values are 0.710 |e| in **L4** and 0.746 |e| in **L5**, indicating that the CT character of transition in these molecules is stronger than the other ones. It should be noted that q_{CT} is the magnitude of the integral of ρ_+ (regions of electronic density increase) and ρ_- (regions of electronic density decrease) over the whole space. It only corresponds to the total amount of charge whose distribution is perturbed during electron excitation; it does not correspond to the net charge transfer from the donor group to the acceptor group.[65] The D_{CT} and q_{CT} are inversely proportional to the HOMO–LUMO energy gap, that is an increase in these CT indices is accompanied by a decrease in VEE and, in turn, an increase in absorption wavelength as observed. In the DMSO solvent, the D_{CT} and q_{CT} indices are smaller than those found in the gas phase, indicating that the absorption wavelength must increase going from the gas phase to DMSO, in good agreement with the $S_0 \rightarrow S_1$ excitation wavelength given in Table 6.

The μ_{CT} (variation in dipole moment between the ground and excited states) can be computed by $\|\mu_{CT}\| = q_{CT}D_{CT}$.[65] Similar to q_{CT} and D_{CT}, due to the larger charge excitation length, the μ_{CT} for **L4** and **L5** is also greater than that for the other molecules in both gas and DMSO media. In addition, μ_{CT} increases going from the gas phase to the DMSO medium.

The H_{CT} is the average degree of spatial extension of hole and electron distribution in the CT direction, and the H index is an overall measure of their extension that represents the half sum of the centroid axis length along the D–A direction. It can be seen from the hole and electron maps in Fig. 9 that both the holes and electrons of the $S_0 \rightarrow S_1$ transition in **L4** and **L5** are distributed in wider regions than in the other molecules. This is why the H indices for these molecules are bigger than the other ones.

The t index represents the difference between the D_{CT} and H_{CT} values. If the t index >0, it means that the ρ_- and ρ_+ regions are significantly separated due to CT. The negative value of the t index indicates that the ρ_- and ρ_+ regions are not substantially separated owing to CT. The t index for **L1**–**L3** is negative and for that **L4** and **L5** is positive so the **L5** molecule has the greatest positive t index, suggesting that the degree of separation of holes and electrons is very low in **L1**–**L3**. Besides, the overlap integral between the ρ_- and ρ_+ regions ($S_\pm$ index) for **L4** and **L5** is less than that for **L1**–**L3**, in agreement with other CT indices.

3.7. AIM analysis and RDG isosurfaces

The strength of intramolecular H-bonding also can be investigated by the topological analysis and the reduced density gradient (RDG) analysis. The topological analysis is based on electron density and is an important part of atoms in molecules theory that was first proposed by Bader.[78,79] The corresponding topological parameters including the electron density $\rho(r)$, the Laplacian of electron density $\nabla^2\rho(r)$, the energy density $H(r)$ and the ratio of $-G(r)/V(r)$ at the bond critical points (BCPs) for ground and excited states are given in Table 10. Here, we focus on the main BCPs at N···H and O···H H-bonds in enol and keto structures, respectively. The value of $\rho(r)$ is strongly related to the strength of IHB. In addition, the potential energy density $V(r)$ highly correlates with the hydrogen bond energy (E_{HB}) which is described as Espinosa's equation: $E_{HB} = 1/2|V(r)BCP|$.[80] From Table 10, the $\rho(r)$ value at the N···H BCP of **L1** to **L5** is 0.0499, 0.0513, 0.0518, 0.0509 and 0.0511 a.u. in the S_0-E state, respectively. The corresponding

value of $\nabla^2\rho(r)$ at the N···H BCP is 0.1163, 0.1168, 0.1173, 0.1171 and 0.1174 a.u. These results show that the intramolecular H-bond strength follows the order: **L3** > **L2** > **L4** > **L5** > **L1**, in good agreement with the calculated H-bonding distances. Based on the $\rho(r)$ and $\nabla^2\rho(r)$ values of **L1**–**L5** at the O···H BCP in the S_0-K state, the IHB strength follows the order **L5** > **L1** > **L4** > **L2** > **L3**. The nature of interactions can be determined in terms of the $\nabla^2\rho(r)$ and $H(r)$. Moreover, the ratio $-G(r)/V(r)$ in the non-covalent nature of the interactions is greater than 1 and that for the covalent nature is smaller than 1. From Table 10, the values of $\nabla^2\rho(r)$ and $H(r)$ at the N···H H-bond critical point (HBCP) of the **L1**–**L5** (R1–5 = –H, –NH_2, –OCH_3, –CF_3, and –CN) compounds are positive and negative, respectively, and the $-G(r)/V(r)$ values are smaller than 1 in both S_0-E and S_0-K states, indicating that the nature of HB interaction in all compounds is partially covalent.

The $\rho(r)$ at the N···H BCP of the **L1**–**L5** molecules at the S_1-E state is 0.0553, 0.0569, 0.0574, 0.0561 and 0.0557 au, respectively, indicating that its value for **L2** and **L3** is greater than that for the other molecules. The comparison of $\rho(r)$ at the N···H BCP reveals that after photoexcitation from S_0-E to S_1-E, the electron density $\rho(r)$ at the N···H BCP of all **L1**–**L5** molecules increases. An increase in $\rho(r)$ at the N···H BCP upon photoexcitation from S_0-E to S_1-E is accompanied by a decrease in $\rho(r)$ at the O–H BCP.

These changes in $\rho(r)$ reveal that the H-bonding interaction is strengthened at the S_1-E state which can promote the proton transfer. The value of E_{HB} is also highly related to the strength of the H-bonding. The larger the value of E_{HB}, the stronger the H-bond. The enhancement in the H-bond strength in the S_1-E state is in the order **L3** > **L2** > **L4** > **L5** > **L1**, in good consistency with the H-bond structural parameters. The sign and values of $\nabla^2\rho(r)$ and $H(r)$ at the N···H BCP in the S_1-E state present an increase in the covalent nature of the N···H BCP under $S_0 \rightarrow S_1$ transition in the enol structures.

Upon the ESIPT process at the S_1 state, the OH···N H-bonding is switched by the O···HN one. The $\rho(r)$ at the O···HN BCP of the **L1**–**L5** molecules at the S_1-K state is 0.0767, 0.0392, 0.0645, 0.0742 and 0.0760 au, respectively, indicating that its value for **L2** and **L3** is less than that for the other molecules. The comparison of the $\rho(r)$ value reveals that the O···HN interaction at the S_1-K state of the molecules is stronger than that of OH···N in the corresponding S_1-E state. The comparison of the values of $\nabla^2\rho(r)$ and $H(r)$ at the O···H BCP shows that the covalent character in the S_1-K structures is greater than that in the S_1-E forms with N···H H-bond interaction.

The non-covalent interaction (NCI) method, which is also known as the reduced density gradient (RDG) method, is a

Table 10 Bond critical point data (in a.u.) in the S_0 and S_1 states for all **L1**–**L5** (R1–5 = –H, NH_2, –OCH_3, –CF_3, and –CN) molecules at the PBE0/6-31++G(d,p) level

	S_0-E		S_1-E		S_0-K		S_1-K	
	O–H	N–H	O–H	N–H	O–H	N–H	O–H	N–H
L1								
$\rho(r)$	0.3291	0.0499	0.3218	0.0553	0.0710	0.2851	0.0767	0.2787
$\nabla^2\rho(r)$	−1.9061	0.1163	−1.8186	0.1210	0.1676	−1.4570	0.1650	−1.4023
$H(r)$	−0.5511	−0.0045	−0.5304	−0.0067	−0.0115	−0.4160	−0.0157	−0.4039
$-G(r)/V(r)$	0.1192	0.8816	0.1250	0.8467	0.8230	0.1106	0.7836	0.1166
E_{HB}		0.0191		0.0218	0.0324		0.0364	
L2								
$\rho(r)$	0.3260	0.0513	0.3183	0.0569	0.0633	0.2936	0.0392	0.3189
$\nabla^2\rho(r)$	−1.8766	0.1168	−1.7835	0.1205	0.1625	−1.5282	0.1046	−1.7376
$H(r)$	−0.5438	−0.0051	−0.5217	−0.0075	−0.0071	−0.4318	−0.0018	−0.4791
$-G(r)/V(r)$	0.1207	0.8710	0.1269	0.8336	0.8711	0.1034	0.9393	0.0853
E_{HB}		0.0197		0.0226	0.0274		0.0274	
L3								
$\rho(r)$	0.3254	0.0518	0.3175	0.0574	0.0595	0.2986	0.0645	0.293
$\nabla^2\rho(r)$	−1.8712	0.1173	−1.7756	0.1207	0.1589	−1.5695	0.1622	−1.5223
$H(r)$	0.5425	−0.0053	−0.5198	−0.0078	0.0595	−0.4412	−0.0078	−0.4306
$-G(r)/V(r)$	0.1210	0.8681	0.1274	0.8299	0.8943	0.0997	0.8414	0.1041
E_{HB}		0.0199		0.0229	0.0252		0.0280	
L4								
$\rho(r)$	0.3275	0.0509	0.3208	0.0561	0.0680	0.2888	0.0742	0.2823
$\nabla^2\rho(r)$	−1.8928	0.1171	−1.8119	0.1216	0.1669	−1.4892	0.1673	−1.4324
$H(r)$	−0.5478	−0.0049	−0.5288	−0.0071	−0.0096	−0.4231	−0.0138	−0.4106
$-G(r)/V(r)$	0.1198	0.8750	0.1255	0.8413	0.8427	0.1071	0.8009	0.1133
E_{HB}		0.0195		0.0223	0.0304		0.0347	
L5								
$\rho(r)$	0.3271	0.0511	0.3216	0.0557	0.0718	0.2842	0.0760	0.2805
$\nabla^2\rho(r)$	−1.8897	0.1174	−1.8240	0.1216	0.1679	−1.4508	0.1676	−1.4167
$H(r)$	−0.5470	−0.0050	−0.5318	−0.0068	−0.0121	−0.4144	−0.0151	−0.4071
$-G(r)/V(r)$	0.1200	0.8733	0.1248	0.8448	0.8176	0.1110	0.7903	0.1151
E_{HB}		0.0197		0.0220	0.0330		0.0361	

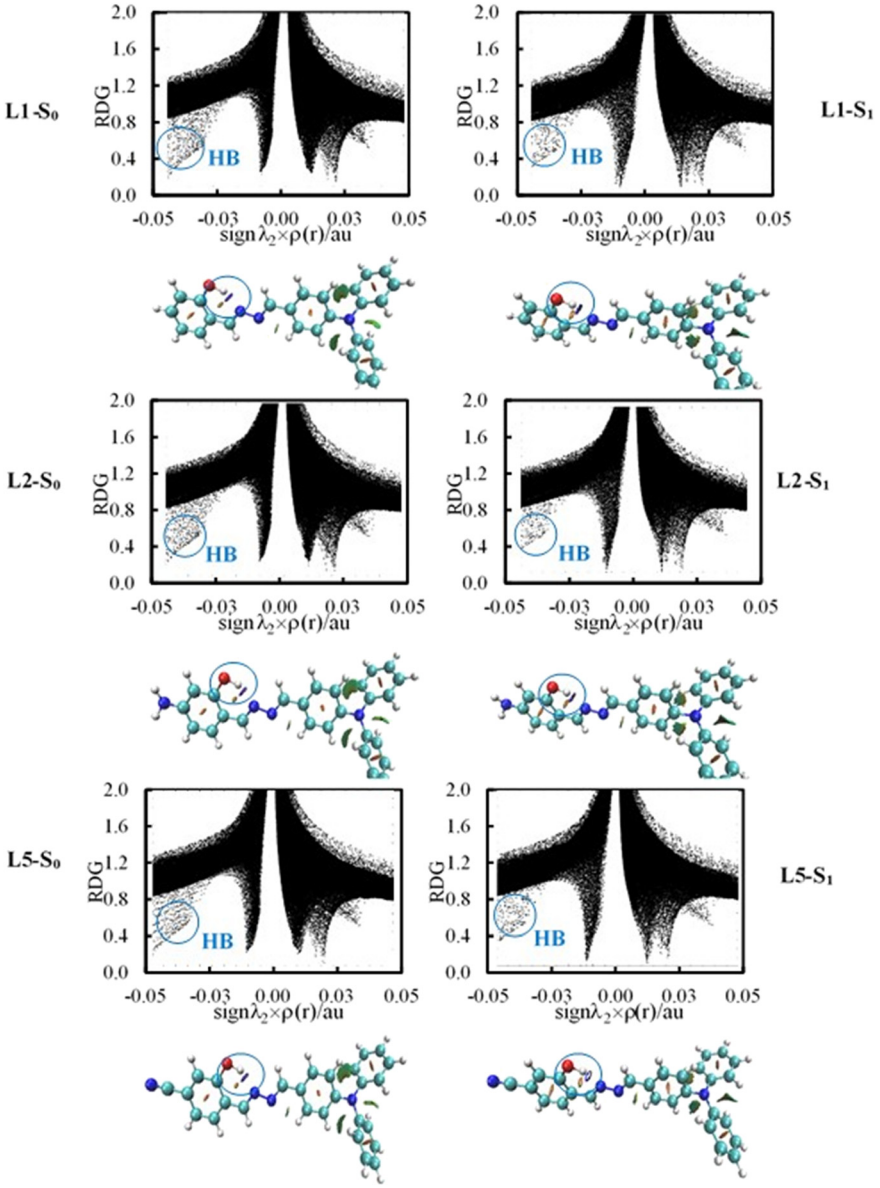

Fig. 8 RDG scatter plots and NCI isosurfaces of **L1**, **L2** and **L5** at the S_0 and S_1 states calculated at PBE0/6-31++G(d,p).

very important method for studying weak interactions.[81] The NCI analysis method can be regarded as an extension of the AIM theory for visual studies. RDG is a simple dimensionless function of the electron density, $\rho(r)$, and its gradient $\nabla\rho(r)$. It can be utilized to elucidate the effect of different factors on the hydrogen bond strength. To further study the IHB in real space, the scatter graphs of the reduced density gradient (RDG) *versus* sign(λ_2)ρ and the corresponding isosurfaces of **L1**, **L2** and **L5** at the S_0 and S_1 states are depicted in Fig. 8, and those of the **L3** and **L4** structures are given in Fig. S6.† The relationship between $\rho(r)$ and $\lambda_2(r)$ is obtained in Bader's theory of atoms in molecules,[59] where $\lambda_2(r)$ represents the second largest eigenvalue of electron density of the Hessian matrix. The sign($\lambda_2(r)$)$\rho(r)$ is the product of the sign of $\lambda_2(r)$ and the electron density of the Hessian matrix at position r. The negative values of sign(λ_2)ρ refer to the H-bonding interactions; positive sign(λ_2)ρ stands for the steric effects and values near zero display the van der Waals (VDW) interactions.[81] The blue circled spike in the RDG isosurfaces shows a strong IHB interaction for these molecules. The spikes located at around −0.05 a.u. for the five molecules in both S_0 and S_1 states confirm the existence of the O–H···N H-bonding interaction in the enol form of the five molecules. In the NCI plots, the light blue color elliptical slab between the oxygen and hydrogen atoms indicates that there is a hydrogen bond.

3.8. NBO charge analysis

To investigate the impact of electron-donating and withdrawing groups on the redistribution of atomic charges in the **L1–L5** (R1–5 = –H, –NH_2, –OCH_3, –CF_3, and –CN)

Table 11 The selected NBO charges (e) of the **L1**–**L5** (R1–5 = –H, –NH_2, –OCH_3, –CF_3, and –CN) molecules at the S_0 and S_1 states in the gas phase at the PBE0/6-31++G(d,p) level

State	q_H	q_N	q_O	q_H	q_N	q_O
	L1			**L2**		
S_0-E	0.5211	−0.3741	−0.7059	0.5216	−0.3912	−0.7082
S_1-E	0.5174	−0.3719	−0.7059	0.5171	−0.3857	−0.7084
S_0-K	0.4672	−0.3817	−0.6937	0.4656	−0.3917	−0.7038
S_1-K	0.4645	−0.3706	−0.6936	0.4609	−0.3659	−0.7183
	L3			**L4**		
S_0-E	0.5225	−0.3864	−0.7071	0.5221	−0.3641	−0.6993
S_1-E	0.5178	−0.3826	−0.7073	0.518	−0.3608	−0.699
S_0-K	0.465	−0.3886	−0.6952	0.4674	−0.3728	−0.6837
S_1-K	0.4627	−0.3758	−0.697	0.4646	−0.3631	−0.6813
	L5					
S_0-E	0.5222	−0.3599	−0.6982			
S_1-E	0.519	−0.358	−0.6974			
S_0-K	0.4681	−0.3686	−0.6849			
S_1-K	0.4652	−0.3612	−0.6805			

compounds and, in turn, on the proton transfer, the NBO charges were calculated at the S_0 and S_1 states in the gas phase at the PBE0/6-31++G(d,p) theoretical level. The selected natural charges of atoms involved in H-bonding interaction are listed in Table 11. The positive charge of the H atom in the S_0-E state increases as **L1** (0.5211 e) < **L2** (0.5216 e) < **L4** (0.5221 e) < **L5** (0.5222 e) < **L3** (0.5225 e) and that in the S_0-K state follows the order: **L3** (0.4650 e) < **L2** (0.4656 e) < **L1** (0.4672 e) < **L4** (0.4674 e) < **L5** (0.4681 e), indicating that the acidity of the H atom in the enol forms is higher than that in the keto ones. The results show that the positive charge on the H atom in the S_1-E state is **L2** (0.5171 e) < **L1** (0.5174 e) < **L3** (0.5178) < **L4** (0.5180 e) < **L5** (0.5190), which are lower than those found at the S_0-E state (**L1** (0.5211 e) < **L2** (0.5216 e) < **L4** (0.5221 e) < **L5** (0.5222 e) < **L3** (0.5225 e)). This indicates that the positive charge of the H atom involved in H-bonding in the gas phase decreases upon photoexcitation from the S_0 to S_1 state. Besides, the positive charge of the H atom at the S_1-K state is in the order **L2** (0.4609 e) < **L3** (0.4627 e) < **L1** (0.4645 e) < **L4** (0.4646 e) < **L5** (0.4652 e), which are smaller than those of the corresponding enol ones at the S_1-E state. Moreover, in both states, the highest positive charge of the H atom corresponds to **L4** and **L5** having electron acceptor groups.

The negative charge of the N atom (q_N) involved in O–H···N H-bonding in the S_0-E state increases in the following order: **L5** (−0.3599 e) < **L4** (−0.3641 e) < **L1** (−0.3741 e) < **L3** (−0.3864 e) < **L2** (−0.3912). It can be seen that the q_N in the **L2** (R = –NH_2) and **L3** (R = –OCH_3) molecules is greater than that in the other molecules. Besides, the presence of two electron-donating groups in both sides of the N–N group in the **L2** and **L3** molecules collectively leads to a greater increase in the electron density of the N atom in the CH═N group of the salicylaldimine moiety and is also involved in O–H···N H-bonding.[36] Upon photoexcitation from S_0-E to S_1-E, the negative charge of the N atom decreases as follows: **L5** (−0.3580 e) < **L4** (−0.3608 e) < **L1** (−0.3717 e) < **L3** (−0.3826 e) < **L2** (−0.3857). Compared with **L1**, the presence of the typical electron-withdrawing groups (–CN and –CF_3) in **L4** and **L5** can attract lone pair electrons of the N atom, thus weakening the ability of the N atom to capture protons. In contrast, introducing the typical electron-donating groups (–NH_2 and –OMe) in **L2** and **L3** has the opposite effect, in good agreement with the lower O–H···N H-bonding distance obtained for **L2** (1.673 Å) and **L3** (1.670 Å) compared with **L4** (1.678 Å) and **L5** (1.681 Å). The results also show that the S_1-E to S_1-K process leads to a decrease and an increase in the negative charge of the N atom in the **L1**–**L3** and **L4**–**L5** molecules, respectively.

The negative charge of atom O involved in hydrogen bonding at the S_0-E state is in the order **L5** (−0.6982 e) < **L4** (−0.6993 e) < **L1** (−0.7059 e) < **L3** (−0.7071 e) < **L2** (−0.7082 e) which changes to **L5** (−0.6974 e) < **L4** (−0.6990 e) < **L1** (−0.7059 e), **L3** (−0.7073 e) and **L2** (−0.7084 e) at the S_1-E state. It is well known that –NH_2 is a better push group than –OMe because of the lower electronegativity of the nitrogen atom; at the same time, the –CN substituent pulls electrons more than –CF_3. Compared with **L1**, the negative charge of the O atom (*i.e.* electronegativity of the O atom) in **L4** and **L5** decreases and that of **L2** and **L3** increases in both states. That is, the ability of the O atom to attract protons in **L4** and **L5** becomes less than that in **L2** and **L3**, in good agreement with the greater O–H bond length obtained for **L2** (1.005 Å) and **L3** (1.006 Å) than for **L4** (1.003 Å) and **L5** (1.001 Å) at the S_1 state. Consequently, the natural charge values of the N and O atoms are in good agreement with the elongation of the O–H bond length and the shortening of the H···N H-bonding distance confirms that the electron-donating substituents can facilitate proton transfer at the S_1 state. Besides, this conclusion is consistent with the electron density at the corresponding BCP.

The negative charge of atom O at the S_1-K state is in the order **L5** (−0.6805 e) < **L4** (−0.6813 e) < **L1** (−0.6936 e) < **L2** (−0.6970 e) < **L3** (−0.7183 e), demonstrating that the highest negative charge value is obtained by adding electron-donating groups. In addition, the negative charge of the O atom decreases upon S_1-E → S_1-K switching. The behaviors of the natural atomic charges of H, O and N involved in proton transfer *versus* RC at the S_1 state for selected **L1**, **L3** and **L5** compounds are illustrated in Fig. 9. It can be seen that the positive charge of the H atom decreases during the PT process. On the other hand, the negative charge of N and O atoms first increases to a minimum and then decreases before relaxing to the keto form. The change in the natural charge of atoms is caused by the change in the structural parameters upon photoexcitation and phototautomerization.

The results of NBO population analysis indicate that the intramolecular charge transfer (ICT) takes place between donor TPA and acceptor salicylaldimine moieties. The sum of atomic natural charges of the donor TPA part can be a good measure of ICT in these molecules. The ICT values in the **L1**–**L5** (R1–5 = –H, –NH_2, –OCH_3, –CF_3, and –CN) molecules are +0.345 e, +0.310 e, +0.002 e, +0.373 e and +0.383 e at the S_0-E state which change to +0.301 e, +0.271 e, −0.042 e, +0.327 e

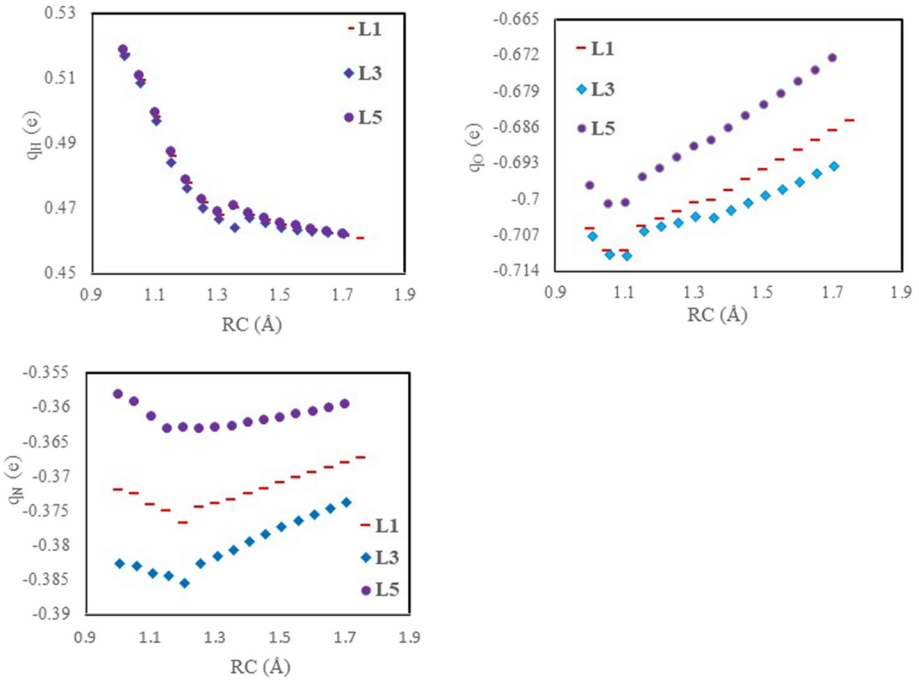

Fig. 9 Changes of the natural atomic charges (H, O and N) in terms of RC along the PT pathway of the selected **L1**, **L3** and **L5** molecules at the S_1 state.

and 0.340 e at the S_1-E state, respectively. The species possesses strong charge transfer (**L4** and **L5**), giving a greater difference in dipole moment between the normal and tautomer forms (1.6 D in the gas phase). The ICT results confirm the electron-donating character of TPA for all **L1**–**L5** at both states, except for **L3** at the S_1 state. As results show, electrons are transferred from the electron-donating TPA part to the electron-accepting part of molecules (except for **L3** at the S_1 state), which leads to the positive charge of the TPA part of molecules, in good agreement with the electron density distribution of the HOMO on the azine and phenol units. Besides, it is found that the ICT value decreases going from the S_0 state to the S_1 one (except for **L3**). In the case of **L3**, the presence of two different electron-donating groups OMe and TPA on both sides of the N–N group nearly prevents ICT from the TPA part of the molecule so the calculated ICT becomes approximately zero (0.002 e at S_0 and −0.014 e at the S_1 sate), compared to the other molecules.

4. Conclusion

In this work, the ESIPT process of a series of donor–acceptor triphenylamine–salicylaldehyde unsymmetrical azine derivatives was investigated by using DFT and TDDFT methods. The effects of different substituents on the photophysical properties of the azine dyes in the gas phase and DMSO, MeOH and toluene solvents were explored. The change in structural parameters, vibrational wavenumbers, electron densities at the BCP, and RDG isosurfaces confirmed that the hydrogen bond interaction is strengthened upon S_0 to S_1 excitation. The greatest H-bonding strength in both states was obtained for **L2** and **L3** having electron-donating groups. The results indicated that the RMSD values for the **L4** and **L5** molecules having electron-withdrawing substituents are greater than those found for the **L1**–**L3** molecules. Constructing the potential energy curves exhibited that the electron-donating and electron-withdrawing substituents could decrease the energy barrier in the first excited state and promote the intramolecular proton transfer compared to the original **L1** molecule. The results indicated that the red shift in the absorption band in the **L4** and **L5** molecules with electron acceptor groups is greater than the other ones. Both S_1-E and S_1-K fluorescence emissions were observed for all studied molecules. The longest emission wavelengths in the gas phase and three solvents are found for **L3** and **L4** with electron-withdrawing groups. Introducing electron-withdrawing groups increases the absorption and emission wavelengths as well as the red shift in fluorescence emission of **L4** and **L5**, but hinders the occurrence of the ESIPT process compared with **L2** and **L3**. The fluorescence rate constants were greater in solution than those in the gas phase. The analysis of frontier molecular orbitals and the hole–electron analysis confirmed the occurrence of ICT during the photoexcitation. The results of NBO charge analysis were in good agreement with the results of H-bonding structural parameters and electron density analysis implying that the ability of the N atom to capture protons in the O–H···N network in **L4** and **L5** is lower than that of **L2** and **L3** at the S_1 state.

Conflicts of interest

There are no conflicts to declare.

References

1 X. Liu, X. Liu, Y. Shen and B. Gu, A simple water-soluble ESIPT fluorescent probe for fluoride ion with large stokes shift in living cells, *ACS Omega*, 2020, **5**(34), 21684–21688.

2 R. Das, S. Bej, H. Hirani and P. Banerjee, Trace-level humidity sensing from commercial organic solvents and food products by an AIE/ESIPT-triggered piezochromic luminogen and ppb-level "OFF–ON–OFF" sensing of Cu^{2+}: a combined experimental and theoretical outcome, *ACS Omega*, 2021, **6**(22), 14104–14121.

3 M. Liu, R. Xiao, B. Feng, D. Fan, S. Huang, A. Bi, S. Zhong, X. Feng, S. Liu and W. Zeng, Elegant cooperation of AIE, ESIPT and ICT effects into tetraarylimidazole-based fluorophore and its tuning for ratiometric detection of carbon monoxide, *Sens. Actuators, B*, 2021, **342**, 130038.

4 T. Samanta, N. Das, D. Patra, P. Kumar, B. Sharmistha and R. Shunmugam, Reaction-triggered ESIPT active water-soluble polymeric probe for potential detection of Hg^{2+}/CH_3Hg^+ in both environmental and biological systems, *ACS Sustainable Chem. Eng.*, 2021, **9**(14), 5196–5203.

5 F. Zeng, G. Bao, B. Zhou and Y. Han, A new fluorescent probe for ultrasensitive detection of phosgene in solution and the gas phase, *New J. Chem.*, 2021, **45**(12), 5631–5636.

6 T. Zhu, Y. Hu, X. Chen, H. Shao, Z. Chen, H. Zhang and C. Liu, Novel chromene-derived fluorescent probe for detection of cyanides by imine-controlled ESIPT, *Dyes Pigm.*, 2021, **195**, 109693.

7 Z. Zong, J. Wang, Y. Bin, Y. Wu and G. Huang, A bifunctional fluorescent probe for sensing of Al 3+ and H 2 S, *Anal. Methods*, 2021, **13**(18), 2157–2164.

8 L. G. Duarte, J. C. Germino, J. F. Berbigier, C. A. Barboza, M. M. Faleiros, D. de Alencar Simoni, M. T. Galante, M. S. de Holanda, F. S. Rodembusch and T. D. Atvars, White-light generation from all-solution-processed OLEDs using a benzothiazole–salophen derivative reactive to the ESIPT process, *Phys. Chem. Chem. Phys.*, 2019, **21**(3), 1172–1182.

9 J. Kumsampao, C. Chaiwai, C. Sukpattanacharoen, T. Chawanpunyawat, P. Nalaoh, P. Chasing, N. Kungwan, T. Sudyoadsuk and V. Promarak, Self-absorption-free excited-state intramolecular proton transfer (ESIPT) emitters for high brightness and luminous efficiency organic fluorescent electroluminescent devices, *Mater. Chem. Front.*, 2021, **5**(16), 6212–6225.

10 V. Trannoy, A. Léaustic, S. Gadan, R. Guillot, C. Allain, G. Clavier, S. Mazerat, B. Geffroy and P. Yu, A highly efficient solution and solid state ESIPT fluorophore and its OLED application, *New J. Chem.*, 2021, **45**(6), 3014–3021.

11 W. Li, P. Chasing, W. Benchaphanthawee, P. Nalaoh, T. Chawanpunyawat, C. Kaiyasuan, N. Kungwan, S. Namuangruk, T. Sudyoadsuk and V. Promarak, Intramolecular hydrogen bond–enhanced electroluminescence performance of hybridized local and charge transfer (HLCT) excited-state blue-emissive materials, *J. Mater. Chem. C*, 2021, **9**(2), 497–507.

12 G. Q. Wei, Y. Yu, M. P. Zhuo, X. D. Wang and L. S. Liao, Organic single-crystalline whispering-gallery mode microlasers with efficient optical gain activated via excited state intramolecular proton transfer luminogens, *J. Mater. Chem. C*, 2020, **8**(34), 11916–11921.

13 M. Durko, G. Ulrich, D. Jacquemin, J. Mysliwiec and J. Massue, Solid-state emitters presenting a modular excited-state proton transfer (ESIPT) process: recent advances in dual-state emission and lasing applications, *Phys. Chem. Chem. Phys.*, 2023, **25**, 15085–15098.

14 A. K. Singh, A. V. Nair, S. S. Shah, S. Ray and N. P. Singh, ESIPT-, AIE-, and AIE+ ESIPT-based light-activated drug delivery systems and bioactive donors for targeted disease treatment, *J. Med. Chem.*, 2023, **66**(6), 3732–3745.

15 B. Roy, R. Mengji, S. Roy, B. Pal, A. Jana and N. P. Singh, NIR-responsive lysosomotropic phototrigger: an "AIE+ ESIPT" active naphthalene-based single-component photoresponsive nanocarrier with two-photon uncaging and real-time monitoring ability, *ACS Appl. Mater. Interfaces*, 2022, **14**(4), 4862–4870.

16 A. Weller, Innermolekularer protonenübergang im angeregten zustand, *Z. Elektrochem.*, 1956, **60**(9–10), 1144–1147.

17 T. D. Krueger, J. Solaris, L. Tang, L. Zhu, C. Webber, R. C. Van Court, S. C. Robinson, O. Ostroverkhova and C. Fang, Illuminating excited-state intramolecular proton transfer of a fungi-derived red pigment for sustainable functional materials, *J. Phys. Chem. C*, 2021, **126**(1), 459–477.

18 W. Yao, T. Deng, A. Huang, Y. Zhang, Q. Li and Z. Li, Promoting photothermal antibacterial activity through an excited-state intramolecular proton transfer process, *J. Mater. Chem. B*, 2023, **11**(24), 5537–5543.

19 J. Hao and Y. Yang, Theoretical Investigation of the Excited-State Dynamics Mechanism of the Asymmetric Two-Way Proton Transfer Molecule BTHMB, *J. Phys. Chem. A*, 2021, **125**(48), 10280–10290.

20 G. Sun and H. Fang, Computational Insights into Sensing Mechanism for Al3+ in a New Acylhydrazone Fluorescent Probe Based on Excited-State Intramolecular Proton Transfer (ESIPT) and Twisted Intramolecular Charge Transfer (TICT), *J. Phys. Chem. A*, 2023, **127**(8), 1857–1865.

21 N. Kanlayakan and N. Kungwan, Molecular design of amino-type hydrogen-bonding molecules for excited-state intramolecular proton transfer (ESIPT)-based fluorescent probe using the TD-DFT approach, *New J. Chem.*, 2021, **45**(28), 12500–12508.

22 H. C. Joshi and L. Antonov, Excited-state intramolecular proton transfer: A short introductory review, *Molecules*, 2021, **26**(5), 1475.

23 R. Liang, Y. Li, Z. Yan, X. Bai, W. Lai, L. Du and D. L. Phillips, Exploring Solvent Effects on the Proton Transfer Processes of Selected Benzoxazole Derivatives by Femtosecond Time-Resolved Fluorescence and Transient Absorption Spectroscopies, *ACS Phys. Chem. Au*, 2022, **3**(2), 181–189.

24 K. Li, Q. Feng, G. Niu, W. Zhang, Y. Li, M. Kang, K. Xu, J. He, H. Hou and B. Z. Tang, Benzothiazole-based AIEgen with

tunable excited-state intramolecular proton transfer and restricted intramolecular rotation processes for highly sensitive physiological pH sensing, *ACS Sens.*, 2018, **3**(5), 920–928.

25 A. C. Sedgwick, L. Wu, H. H. Han, S. D. Bull, X. P. He, T. D. James, J. L. Sessler, B. Z. Tang, H. Tian and J. Yoon, Excited-state intramolecular proton-transfer (ESIPT) based fluorescence sensors and imaging agents, *Chem. Soc. Rev.*, 2018, **47**(23), 8842–8880.

26 P. Zhou and K. Han, ESIPT-based AIE luminogens: Design strategies, applications, and mechanisms, *Aggregate*, 2022, **3**(5), e160.

27 S. S. Chourasiya, D. Kathuria, A. A. Wani and P. V. Bharatam, Azines: Synthesis, structure, electronic structure and their applications, *Org. Biomol. Chem.*, 2019, **17**(37), 8486–8521.

28 S. Guieu, F. Cardona, J. Rocha and A. M. Silva, Tunable Color of Aggregation-Induced Emission Enhancement in a Family of Hydrogen-Bonded Azines and Schiff Bases, *Chem. – Eur. J.*, 2018, **24**(65), 17262–17267.

29 Y. Shen, M. Li, M. Yang, Y. Zhang, H. Li and X. Zhang, A specific AIE and ESIPT fluorescent probe for peroxynitrite detection and imaging in living cells, *Spectrochim. Acta, Part A*, 2019, **222**, 117230.

30 H. Song, Y. Zhou, H. Qu, C. Xu, X. Wang, X. Liu, Q. Zhang and X. Peng, A novel AIE plus ESIPT fluorescent probe with a large Stokes shift for cysteine and homocysteine: application in cell imaging and portable kit, *Ind. Eng. Chem. Res.*, 2018, **57**(44), 15216–15223.

31 S. Khanra, S. Ta, M. Ghosh, S. Chatterjee and D. Das, Subtle structural variation in azine/imine derivatives controls Zn 2+ sensitivity: ESIPT-CHEF combination for nano-molar detection of Zn^{2+} with DFT support, *RSC Adv.*, 2019, **9**(37), 21302–21310.

32 A. A. Bhosle, S. D. Hiremath, A. C. Bhasikuttan, M. Banerjee and A. Chatterjee, Solvent-free mechanochemical synthesis of a novel benzothiazole-azine based ESIPT-coupled orange AIEgen for the selective recognition of Cu2+ ions in solution and solid phase, *J. Photochem. Photobiol., A*, 2021, **413**, 113265.

33 M. Mathivanan and B. Murugesapandian, Substitution dependent multi-color AIE behavior and ESIPT active ADA type triphenylamine supported bis unsymmetrical azine derivatives and their antibacterial activity, *Dyes Pigm.*, 2022, **203**, 110367.

34 S. H. Ramugade, U. S. Warde and N. Sekar, Azo dyes with ESIPT core for textile applications and DFT study, *Dyes Pigm.*, 2019, **170**, 107626.

35 J. Tong, K. Zhang, J. Wang, H. Li, F. Zhou, Z. Wang, X. Zhang and B. Z. Tang, Keto-salicylaldehyde azine: asymmetric substituent effect on their optical properties via electron-donating group insertion, *J. Mater. Chem. C*, 2020, **8**(3), 996–1001.

36 M. Mathivanan, B. Tharmalingam, C. H. Lin, B. V. Pandiyan, V. Thiagarajan and B. Murugesapandian, ESIPT-active multi-color aggregation-induced emission features of triphenylamine–salicylaldehyde-based unsymmetrical azine family, *CrystEngComm*, 2020, **22**(2), 213–228.

37 J. Zhao, Z. Li and B. Jin, Uncovering photo-induced hydrogen bonding interaction and proton transfer mechanism for the novel salicylaldehyde azine derivative with para-position electrophilic cyano group, *J. Lumin.*, 2021, **238**, 118231.

38 P. Gayathri, S. Ravi, K. Akshaya, S. Karthikeyan, M. Pannipara, A. G. Al-Sehemi, D. Moon and S. P. Anthony, ESIPT geometrical isomers with distinct mechanofluorochromism and intra/intermolecular H-bonding controlled tunable fluorescence, *CrystEngComm*, 2022, **24**(46), 8126–8133.

39 A. Jain, S. De and P. Barman, Salicylaldehyde-diphenyl-azine skeleton-based ESIPT-coupled AIEgens with tunable emission and applicable as highly selective and sensitive Cu2+ ion sensor, *Dyes Pigm.*, 2023, **220**, 111769.

40 T. Mondal, S. Biswas, M. V. Mane and S. S. Panja, Deciphering swift reversal of multifaceted photodynamics of a novel pyrene appended unsymmetrical salicylaldehyde azine derivative in aqueous and protein environments, *New J. Chem.*, 2023, **47**(11), 5280–5300.

41 H. Roohi and T. Pouryahya, TD-DFT study of the excited state intramolecular proton transfer (ESIPT) mechanism and photophysical properties in coumarin–benzothiazole derivatives: substitution and solvent effects, *Mol. Syst. Des. Eng.*, 2023, **8**(5), 647–665.

42 C. Adamo and D. Jacquemin, The calculations of excited-state properties with Time-Dependent Density Functional Theory, *Chem. Soc. Rev.*, 2013, **42**(3), 845–856.

43 R. G. Parr and W. Yang, *Density-functional theory of atoms and molecules*, Oxford Univ. Press, New York, 1989.

44 Y. Zhao and D. G. Truhlar, Density functionals with broad applicability in chemistry, *Acc. Chem. Res.*, 2008, **41**(2), 157–167.

45 A. D. Laurent and D. Jacquemin, TD-DFT benchmarks: a review, *Int. J. Quantum Chem.*, 2013, **113**(17), 2019–2039.

46 T. Yanai, D. P. Tew and N. C. Handy, A new hybrid exchange–correlation functional using the Coulomb-attenuating method (CAM-B3LYP), *Chem. Phys. Lett.*, 2004, **393**(1–3), 51–57.

47 C. Adamo and V. Barone, Toward reliable density functional methods without adjustable parameters: The PBE0 model, *J. Chem. Phys.*, 1999, **110**(13), 6158–6170.

48 F. Jensen, *Introduction to computational chemistry*, John wiley & sons, 2017.

49 M. J. Frisch, *et al.*, *Gaussian 16, Revision A. 03*, Gaussian, Inc., Wallingford CT, 2016.

50 D. J. Tozer, Relationship between long-range charge-transfer excitation energy error and integer discontinuity in Kohn–Sham theory, *J. Chem. Phys.*, 2003, **119**(24), 12697–12699.

51 B. Champagne, V. Liégeois and F. Zutterman, Pigment violet 19—a test case to define a simple method to simulate the vibronic structure of absorption spectra of organic pigments and dyes in solution, *Photochem. Photobiol. Sci.*, 2015, **14**(2), 444–456.

52 O. Louant, B. Champagne and V. Liégeois, Investigation of the Electronic Excited-State Equilibrium Geometries of Three Molecules Undergoing ESIPT: A RI-CC2 and TDDFT Study, *J. Phys. Chem. A*, 2018, **122**(4), 972–984.
53 M. Miura, Y. Aoki and B. Champagne, Assessment of time-dependent density functional schemes for computing the oscillator strengths of benzene, phenol, aniline, and fluorobenzene, *J. Chem. Phys.*, 2007, **127**(8), 084103.
54 M. R. Silva-Junior, M. Schreiber, S. Sauer and W. Thiel, Benchmarks for electronically excited states: Time-dependent density functional theory and density functional theory based multireference configuration interaction, *J. Chem. Phys.*, 2008, **129**(10), 104103.
55 R. Sarkar, M. Boggio-Pasqua, P. F. Loos and D. Jacquemin, Benchmarking TD-DFT and wave function methods for oscillator strengths and excited-state dipole moments, *J. Chem. Theory Comput.*, 2021, **17**(2), 1117–1132.
56 M. Cossi, V. Barone, B. Mennucci and J. Tomasi, Ab initio study of ionic solutions by a polarizable continuum dielectric model, *Chem. Phys. Lett.*, 1998, **286**(3–4), 253–260.
57 H. Roohi and N. Abdollahinezhad, Photo-induced proton transfer in fluorene-and carbazole-based compounds as red-and orange-light-emitting molecules: A TD-DFT study, *Org. Electron.*, 2015, **25**, 121–130.
58 H. Roohi, R. Nokhostin and M. Mohamadnia, Photoswitching in nanostructured benzofuro [3, 2-b] pyridin-9-ol and benzothio [3, 2-b] pyridin-9-ol compounds as red-and yellow-light-emitting molecules: A TD-DFT approach, *Dyes Pigm.*, 2016, **134**, 106–117.
59 R. Bader, *Atoms in molecules: a quantum theory*, Oxford Univ. Press., Oxford, 1990.
60 R. F. Bader, Bond paths are not chemical bonds, *J. Phys. Chem. A*, 2009, **113**(38), 10391–10396.
61 F. Biegler-Konig, J. Schonbohm and D. Bayles, Software news and updates-AIM2000-A program to analyze and visualize atoms in molecules, *J. Comput. Chem.*, 2001, **22**(5), 545–559.
62 E. R. Johnson, S. Keinan, P. Mori-Sánchez, J. Contreras-García, A. J. Cohen and W. Yang, Revealing noncovalent interactions, *J. Am. Chem. Soc.*, 2010, **132**(18), 6498–6506.
63 T. Lu and F. Chen, Multiwfn: A multifunctional wavefunction analyzer, *J. Comput. Chem.*, 2012, **33**(5), 580–592.
64 W. Humphrey, A. Dalke and K. Schulten, VMD: visual molecular dynamics, *J. Mol. Graphics*, 1996, **14**(1), 33–38.
65 T. Le Bahers, C. Adamo and I. Ciofini, A qualitative index of spatial extent in charge-transfer excitations, *J. Chem. Theory Comput.*, 2011, **7**(8), 2498–2506.
66 E. D. Glendening, C. R. Landis and F. Weinhold, Natural bond orbital methods, *Wiley Interdiscip. Rev.: Comput. Mol. Sci.*, 2012, **2**(1), 1–42.
67 A. E. Reed, L. A. Curtiss and F. Weinhold, Intermolecular interactions from a natural bond orbital, donor-acceptor viewpoint, *Chem. Rev.*, 1988, **88**(6), 899–926.
68 K. C. Tang, M. J. Chang, T. Y. Lin, H. A. Pan, T. C. Fang, K. Y. Chen, W. Y. Hung, Y. H. Hsu and P. T. Chou, Fine tuning the energetics of excited-state intramolecular proton transfer (ESIPT): white light generation in a single ESIPT system, *J. Am. Chem. Soc.*, 2011, **133**(44), 17738–17745.
69 Z. Zhang, Y. A. Chen, W. Y. Hung, W. F. Tang, Y. H. Hsu, C. L. Chen, F. Y. Meng and P. T. Chou, Control of the reversibility of excited-state intramolecular proton transfer (ESIPT) reaction: host-polarity tuning white organic light emitting diode on a new thiazolo [5, 4-d] thiazole ESIPT system, *Chem. Mater.*, 2016, **28**(23), 8815–8824.
70 K. I. Sakai, H. Kawamura, N. Kobayashi, T. Ishikawa, C. Ikeda, T. Kikuchi and T. Akutagawa, Highly efficient solid-state red fluorophores using ESIPT: crystal packing and fluorescence properties of alkoxy-substituted dibenzothiazolylphenols, *CrystEngComm*, 2014, **16**(15), 3180–3185.
71 H. Roohi and P. Alizadeh, Fine tuning the emission wavelengths of the 7-hydroxy-1-indanone based nano-structure dyes: Near-infrared (NIR) dual emission generation with large stokes shifts, *Spectrochim. Acta, Part A*, 2018, **196**, 83–102.
72 Q. Huang, Q. Guo, J. Lan, R. Su, Y. Ran, Y. Yang, Z. Bin and J. You, Mechanically induced single-molecule white-light emission of excited-state intramolecular proton transfer (ESIPT) materials, *Mater. Horiz.*, 2021, **8**(5), 1499–1508.
73 L. Zhang, G. H. Peslherbe and H. M. Muchall, Ultraviolet absorption spectra of substituted phenols: a computational study, *Photochem. Photobiol.*, 2006, **82**(1), 324–331.
74 J. B. Barbour and J. M. Karty, Resonance and field/inductive substituent effects on the gas-phase acidities of para-substituted phenols: a direct approach employing density functional theory, *J. Phys. Org. Chem.*, 2005, **18**(3), 210–216.
75 M. Palusiak and T. M. Krygowski, Application of AIM Parameters at Ring Critical Points for Estimation of π-Electron Delocalization in Six-Membered Aromatic and Quasi-Aromatic Rings, *Chem. – Eur. J.*, 2007, **13**(28), 7996–8006.
76 J. M. Hollas, *Modern spectroscopy*, John Wiely&Sons Ltd, 1995.
77 L. Huet, A. Perfetto, F. Muniz-Miranda, M. Campetella, C. Adamo and I. Ciofini, General density-based index to analyze charge transfer phenomena: From models to butterfly molecules, *J. Chem. Theory Comput.*, 2020, **16**(7), 4543–4553.
78 R. F. Bader, Atoms in molecules, *Acc. Chem. Res.*, 1985, **18**(1), 9–15.
79 R. F. Bader, A quantum theory of molecular structure and its applications, *Chem. Rev.*, 1991, **91**(5), 893–928.
80 E. Espinosa, E. Molins and C. Lecomte, Hydrogen bond strengths revealed by topological analyses of experimentally observed electron densities, *Chem. Phys. Lett.*, 1998, **285**(3–4), 170–173.
81 E. R. Johnson, S. Keinan, P. Mori-Sánchez, J. Contreras-García, A. J. Cohen and W. Yang, Revealing noncovalent interactions, *J. Am. Chem. Soc.*, 2010, **132**(18), 6498–6506.

